CHAPTER 4

Analysis

In this chapter, the details of antiproton analysis will be given, including all the steps of deriving the time averaged and time dependent antiproton to proton flux ratio. To determine the flux ratio, the definition of flux should be given first. In general, the flux is calculated by:

$$\Phi(|R|) = \frac{N(|R|)}{\Delta R \cdot T(|R|) \cdot A(|R|) \cdot \epsilon(|R|)} \tag{4.1}$$

where $N(|R|)$ is the event count numbers, ΔR is the rigidity bins, $T(|R|)$ is the measuring time, and the $\epsilon(|R|)$ is the trigger efficiency, $A(|R|)$ is the effective acceptance. All the rigidity should be the true rigidity of the event, while the event number from the template fit is obtained as a function of reconstructed rigidity. Therefore unfolding procedure should be done regarding this issue. This will be discussed further in section 4.8.

In section 4.1, the data reconstruction and selection is discussed. Section 4.2 shows the construction of charge confusion estimator. Section 4.3 describes how the TRDlikelihood estimator is constructed. In section 4.4, the template fit procedures to get the antiproton signals in different rigidity ranges are shown. Section 4.5 gives the detail about how to calculate the effective acceptances of antiproton and proton. In section 4.6, the measuring time used in this analysis is determined. In section 4.7, the trigger efficiency used in this analysis is calculated. Section 4.8 shows the unfolding procedure. In section 4.9, the formula for calculation of antiproton to proton flux ratio is derived. In section 4.10, the different systematic uncertainties in different rigidity ranges are discussed.

4.1. Data Selection

4.1.1. AMS-02 Data and Monte Carlo Simulation

This section shows the data used in this analysis and the complete list of cuts and selections. In this analysis, the used AMS-02 experiment data is collected from 20.May 2011 to 03.May 2021. Raw collected data need some calibration and alignment work and then could be reconstructed via AMS-02 official software (named gbatch), resulting in the analysis data stored in ROOT file format. The ROOT data analysis format is developed at CERN that is dedicated for High energy particle physics analysis [88] . Furthermore, a software developed in Aachen called ACSoft is used to generate data in a higher-level structure called ACQT [89] . The analysis in this thesis is based on the pass7 version data (reconstructed via gbatch in version B1130).

The rigidity bin used in this analysis is the same as the one used in the previous AMS-02 proton analysis [90] , which is determined by rigidity resolution. In rigidity higher than 80.5 GV, the rigidity bins are merged in every two bins to increase antiproton statistics.

The sun is not a solid body but is made of gas plasma. Due to the solar rotations, different latitudes would show different rotation periods. From the view of the Earth, the solar rotations can be quantified with the Bartels Rotation Numbers. The Bartels Rotation Numbers is exactly 27 days, close to the synodic rotation period [91] . The starting counting was from 8th Feb 1832, and this day was arbitrarily assigned by Julius Bartels.

For time dependent analysis, the collected ISS data is divided into six Bartels Rotations time bins. Because of the rigidity cutoff, the statistic in the low rigidity range in each time interval is limited. Therefore, the rigidity bins are merged in every two original time averaged rigidity bins in time dependent antiproton analysis. The data collection used in this thesis started in May 2011, which is Bartels Rotation 2426, and ended in May 2021, which is Bartels Rotation 2561. In total, the data can be divided into 23 intervals of six Bartels Rotations though the last time bin has less data than the full six Bartels Rotations.

Due to the technical problems in tracker pumps and a repair mission for new TTCS systems from Nov 2019 to Jan 2020, the operation mode frequently changed during some periods and the tracker had to turn off. In those periods, the data taking was excluded and not used in this analysis.

To validate the sub detector's performance and study the detector's operation, an extensive set of MC simulations has been done by the AMS-02 collaboration with the help of the Geant4 framework [92, 93] . This includes the interaction with all the sub-detectors and their support structure. In this thesis, all the AMS-02 MC events are generated from the top of the experiment with a 3.9 meters plane, the solid angle of the generated event is $\pi \cdot$sr, and the generated momentum spectrum is either a power law with spectrum index -2.7 or a constant in $\log(p)$ axis. By comparing the data distributions in different variables, the sub-detectors response for different cosmic rays can be systematically studied.

In this thesis, the used MC datasets are protons, antiprotons, and electrons. They are generated in different momentum ranges for various purposes. For example, one of the main purposes of using MC proton data in this analysis is to study proton charge confusion, which is proton events but measured with the wrong rigidity sign. The reasons are finite tracker rigidity resolution and the interactions with the sub-detectors [94] . By selecting the negative rigidity data samples from the proton MC dataset, the proton charge confusion data can be selected. More detail will be discussed in 4.2. Some other usages like calculating effective acceptance and determining the systematic uncertainties due to acceptance will be shown in detail later in this chapter.

For the simulated MC events, the generated momentum spectrum does not perfectly match the realistic spectrum. This could introduce bias in some variable distributions in MC. In order to correct this, the weight of MC events should be reassigned by calculating the ratio of event counts over reference flux. For example, the re-weighting of the proton MC dataset uses AMS-02 published proton flux result [90] as reference flux. The re-weighting factor can be obtained by dividing the MC event count by reference event counts in each rigidity bin. The acquired re-weighting factor will be used in filling variable histograms for further procedure.

Up to May 2021, the AMS-02 experiment has collected more than 174 billion cosmic rays events. To select antiproton events from them, cuts and selections must be put on first. There are two levels of selection, the first is the preselection, and the second is the selection. In the next few subsections, the definition of all selections and passing ratios will be given.

4.1.2. Preselection Cuts

The first level of cuts and selections is preselection. The purpose is to discard data taken in bad sub-detectors operations or in bad quality. These selections are general and should be applied before any cosmic ray component analyses. The preselection consists of two parts: data taking quality cuts and analysis data quality cuts.

Data taking quality cuts require all the sub-detectors running in nominal conditions, and the data taking condition is normal. The first one excludes the period that any sub-detector has some special operations or tests. For example, the TRD gas refill takes place around every month. In this period, the data taken is not included in this analysis. The second one requires that the data taking period is normal. For instance, if the ISS is in the South Atlantic Anomaly (SAA) area, the data taken in this period is not included in this analysis. In summary, the table of 4.1 shows the pass ratio of all the data taking quality cuts.

After the data taking quality cuts, all the pass data are taken in the normal operation period. But for analysis, further quality selections are needed to ensure the analysis based on these data is meaningful. The analysis data quality cuts are used to discard the low quality

Table 4.1: List of data taking quality cuts

Cuts	Description	Pass Ratio
Bad Runs	Remove events in bad sub-detecter status	99.73 %
Second Within Run	Remove events without a run ID	99.92 %
Bad Reconstruction Period	Remove events with bad reconstruction efficiency	95.15 %
Bad Facing Angle	Remove events in rotated ISS status	99.78 %
No Missed Events	Remove seconds with more than 10% events missing	99.91 %
Bad Live Time	Remove seconds with live time fraction (see section 4.6) < 0.5	95.67 %
Too Many Events In Second	Remove seconds with too many events	97.86 %
Good Alignment	Remove events without good alignment	99.86 %
High TRD Occupancy Period	Remove events with too high TRD occupancy	97.80 %
No Hardware Errors	Remove events with hardware errors	99.91 %

collected data then the analysis is based on relatively golden data. In 4.2, the complete list of analysis data quality cuts and the correspondent pass ratios are shown.

Table 4.2: List of analysis data quality cuts

Cuts	Pass Ratio
Has TOF Beta Measurement	68.02 %
Particle is Downgoing	88.03 %
Has Hits in Central Inner Tracker	70.16 %
Has Single Tracker Track	61.01 %
Tracker Track Fit Chi2 in X	97.33 %
Tracker Track Fit Chi2 in Y	90.64 %
Has Hits in all four TOF Layers	89.44 %

- The **Has TOF Beta Measurement** requires that the TOF beta measurement is available. The TOF beta is used to separate antiproton signals and backgrounds in low rigidity ranges.

- The **Particle is Downgoing** is the cut on particle going direction. By requiring TOF beta measurement is positive, the particle going from upper TOF to lower TOF is selected.

- The **Has Hits in Central Inner Tracker** requires hits in tracker layer 3 or 4, 5 or 6, 7 or 8. To have an accurate rigidity measurement, the tracker hits inside the magnet is necessary. Therefore central inner tracker should have enough hits to construct the rigidity.

- The **Has Single Tracker Track** requires that for each event, only one reconstructed tracker track is found. To avoid multiple tracker tracks produced by interaction, this analysis only uses single tracker track events.

- The **Tracker Track Fit Chi2 in X** and **Tracker Track Fit Chi2 in Y** are the cuts on tracker track fit Chi2 less than 10 in X and Y directions respectively. To ensure the events used for analysis have good tracker track fit and rigidity correspondently, the cuts on Chi2 in bending and unbending directions are mandatory.

- The **Has Hits in all four TOF Layers** requires that all the four TOF layers have hits. Since the TOF provides trigger and also the beta measurement, hits on all four TOF layers give a precise response of TOF.

4.1.3. Quality Cuts

The preselection is independent of the analysis topic. For the antiproton to proton ratio analysis, some dedicated selections need to be applied further. These cuts are mainly used to select charge one particle and ensure good quality analysis events. To have good quality analysis variables like particle charge or beta, the basic reconstruction of events needs to be done with the minimum response of sub-detectors. In 4.3, the table shows all the selections used in this analysis.

Table 4.3: List of quality cuts

Cuts	Pass Ratio
Tracker Charge Cut	87.16%
Upper TOF Charge Cut	97.46%
Lower TOF Charge Cut	97.22%
TRD Number Of Raw Hits Cut	98.89%
TRD Active Layers Cut	90.71%
Tracker Track In Trd Acceptance Cut	87.48%
TRD TOF Track Match XY Cut	96.76%

- The **Tracker Charge Cut** is the cut on the inner tracker charge measurement. With the cut $0.7 <$ inner tracker charge < 1.3, the charge one particle is selected from the tracker. In the low rigidity analysis, the hits on the tracker track L1 and L9 are not required. Therefore only the charge measurement in the inner tracker is guaranteed.

- The **Upper TOF Charge Cut** is the cut on upper TOF charge measurement. The lower value is 0, which cuts away the bad charge reconstruction events, and the higher value is 1.5, which cuts away charge two and higher events.

- The **Lower TOF Charge Cut** is the cut on lower TOF charge measurement. The lower limit is 0 and the higher limit is 2. Due to the possible interaction between the two TOF layers, the cut value on lower TOF is wider than on upper TOF.

- The **TRD Number Of Raw Hits Cut** requires $8 <$ TRD Number Of Raw Hits $<$

1000. To have a minimum response of TRD, the minimum cuts on TRD raw hits are necessary. This ensures a good reconstruction of TRD variables.

- The **TRD Active Layers Cut** requires 14 < TRD Active Layers < 20. To ensure a good TRD measurement of the event and construct the TRDLikelihood precisely, a minimum of TRD active layers is required.

- The **Tracker Track In Trd Acceptance Cut** requires that the tracker track of the event is inside TRD's geometrical acceptance. Therefore, the tracker track produced from the side or from interaction could be reduced.

- The **TRD TOF Track Match XY Cut** cut on the distance between the TRD track and the TOF track less than 40 cm. This ensures that the TRD track and TOF track are consistent with each other and a clean traverse path is obtained.

4.2. Charge Confusion Estimator

Due to the finite rigidity resolution or the interactions with the AMS sub-detectors, protons could be misconstructed with opposite rigidity signs. This is called "Charge Confused Protons". The charge confused protons can mimic the behavior of charge correct antiprotons. Therefore, the charge confused protons can go into the antiproton signal ranges when determining the antiprotons. With the rigidity going up, the wrongly reconstructed protons increase dramatically. So in the high rigidity range, most backgrounds of antiproton signals are charge confused protons.

To solve this problem, the machine learning technique is used. The separation of antiproton signals and charge confused protons depends on the sign of rigidity. Since there are only two possible categories: positive rigidity and negative rigidity, the case falls into a binary classification. After checking the data/MC matching, the proton MC simulation data can be used in this learning process. In summary, the charge confusion proton case is supervised learning with two categories.

To train the charge confusion classifier estimator, variables containing relevant information should be used. In this analysis, 16 variables from the sub-detectors are used for training. Most variables are from the tracker, and the others are from the TOF and the TRD. These variables are constructed by summarising the characters of charge confused proton events and are also used in previous AMS-02 antiproton analyses [50] .

The training samples are taken from proton MC simulation. By selecting the negative rigidity events from proton MC data in the absolute rigidity above around 20 GV, the charge confused protons can be obtained. Since the antiproton and proton only have charge differences, the antiproton's behavior in sub-detectors is assumed to be the same as the proton's, but only the rigidity sign is opposite. The charge correct antiproton samples can be replaced by charge correct proton samples but with opposite rigidity signs.

In the appendix A, the complete list of all the 16 variables and their definitions are shown. In figure 4.1, the four most important variables and their responses are given as examples to illustrate the information of separating the charge correct signal and charge confused background.

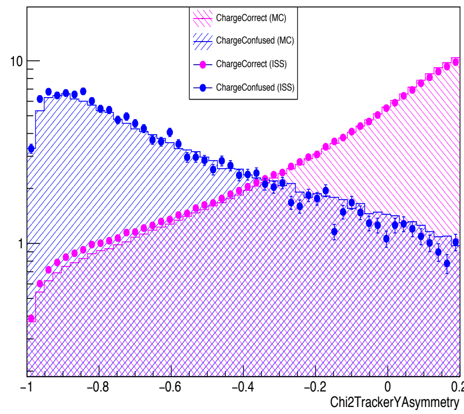

(a)

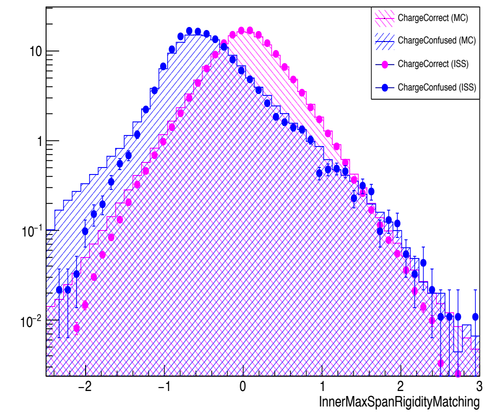

(b)

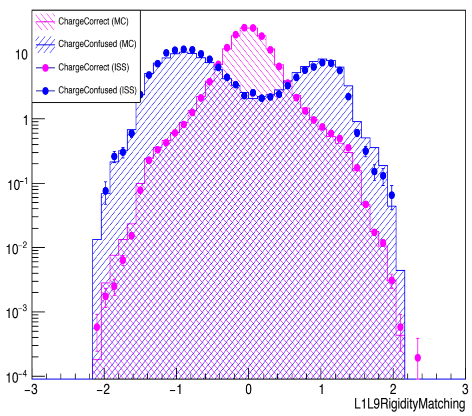

(c)

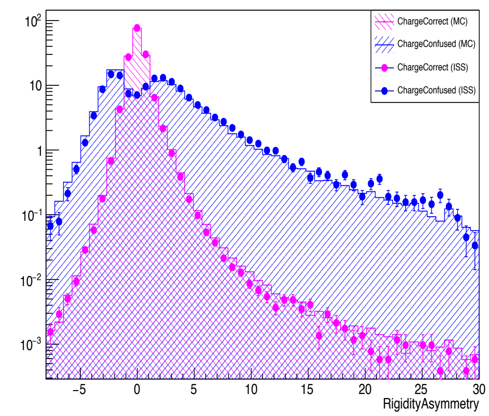

(d)

Figure 4.1: Four most important input variables used for training the charge confusion estimator: a). **Chi2TrackerYAsymmetry** b). **InnerMaxSpanRigidityMatching** c). **L1L9RigidityMatching** d). **RigidityAsymmetry**. The points are collected data, and the histograms are proton MC simulation. The pink is the distribution for the charge correct antiprotons, and the blue is the distribution for the charge confused protons.

The definitions of the four variables are given here:

1 **RigidityAsymmetry** $= \frac{\text{RigidityInnerL1}-\text{RigidityInnerL9}}{\text{RigidityInnerL1}+\text{RigidityInnerL9}}$. The RigidityInnerL1 is the rigidity reconstructed with only the hits in the inner tracker layers and tracker layer 1. The RigidityInnerL9 is the rigidity reconstructed with only the hits in the inner tracker

layers and tracker layer 9.

2 **Chi2TrackerYAsymmetry** $= \frac{\text{Chi2TrackerYInner}-\text{Chi2TrackerY}}{\text{Chi2TrackerYInner}+\text{Chi2TrackerY}}$. The Chi2TrackerYInner is the Chi2 of the Y side tracker track fitting only from the inner tracker layers. The Chi2TrackerY is the Chi2 of the Y side tracker track fitting from all the tracker layers.

3 **InnerMaxSpanRigidityMatching** $= 100 \cdot \left[\left(\frac{1.0}{\text{RigidityInner}}\right) - \left(\frac{1.0}{\text{Rigidity}}\right)\right] \cdot \frac{\text{R}}{|\text{R}|}$. The RigidityInner is the rigidity reconstructed only with the hits in the inner tracker layers. The Rigidity is the rigidity reconstructed with the hits in all the tracker layers.

4 **L1L9RigidityMatching** $= 100 \cdot \left[\left(\frac{1.0}{\text{RigidityInnerL1}}\right) - \left(\frac{1.0}{\text{RigidityInnerL9}}\right)\right] \cdot \frac{\text{R}}{|\text{R}|}$. The RigidityInnerL1 and RigidityInnerL9 have been defined in the previous value.

From the figure, we could see that the data and MC have similar distributions. This is important for further steps. The estimator training process is based on MC data. In order to make sure the trained estimator is applicable for data, the distributions of MC and data have to match with each other.

All four variables contain information about the differences between signal and background. From the figure, the differences between signal distribution and background distribution are easy to observe. These differences are used for the further training process.

In the TMVA framework [95] , there are different training methods provided, like Boosted Decision Tree (BDT), Support Vector Machine (SVM), Gradient Tree Boosting (GTB), or Likelihood method. To achieve the best separation performance, all the methods have been tried to get the best separation power. In this analysis, the Boosted Decision Tree (BDT) is used as the default method since it provides the best separation between signals and backgrounds.

The proton MC data is divided into positive and negative parts with the same amount of events. Each part is divided into train sample, validation sample, and test sample with a ratio of 6:3:1. To avoid overtraining, the training process requires the response on the training sample should be the same as the response on the validation sample.

After training, the *charge confusion estimator* is obtained. In figure 4.2, the separation between charge correct antiproton signals and charge confused proton backgrounds in an example rigidity bin of 147-175 GV can be seen. The peak at 1 means the charge correct events, and the peak at 0 means the charge confused events. By setting a cut on the charge confusion estimator, the charge correct antiproton samples can be obtained. But in this way, some antiproton signals would still be lost and some backgrounds go into the signal range. Therefore, a template fit method is required to get the signal numbers precisely. This will be shown in section 4.4.

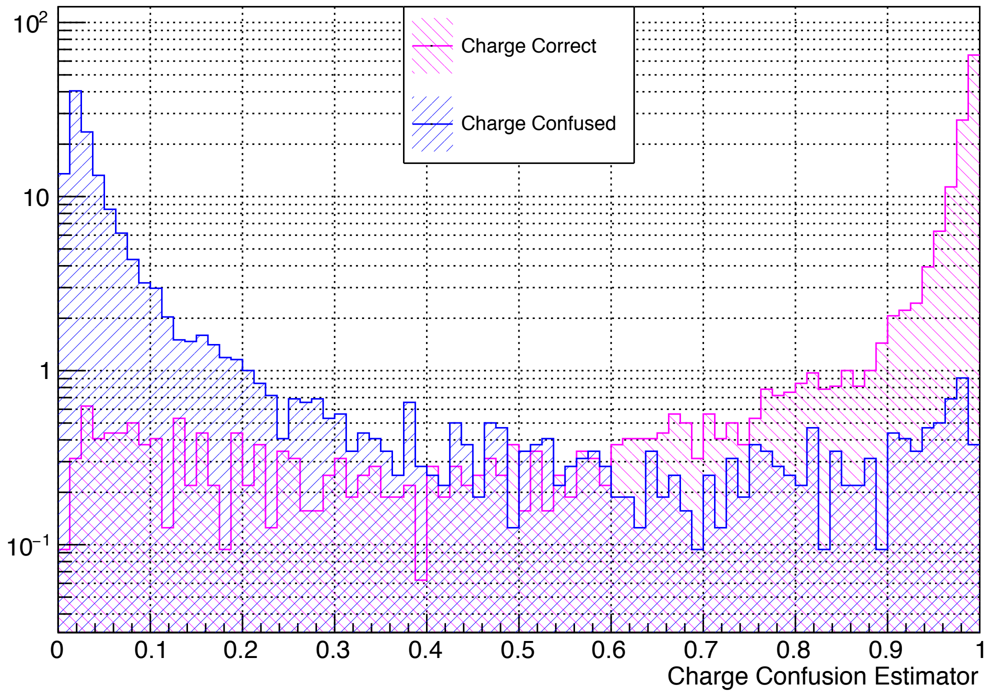

Figure 4.2: The charge confusion estimator response on charge correct antiprotons (pink) and charge confused protons (blue) in 147-175 GV

4.3. TRD Estimator

Except for the charge confusion estimator, another estimator to be constructed before the antiproton signal determination is the TRDLikelihood estimator. The charge confusion estimator is constructed to separate charge confused protons backgrounds, while the TRDLikelihood estimator is constructed to separate light particle backgrounds like electrons.

As introduced in section 3.2, the TRD sub-detector has the power to separate the heavy and light particles. When the protons (antiprotons) pass the tubes of TRD, they leave dE/dX signals. For the electrons, due to the high Lorenz factor, they emit transition radiation, which can be used to distinguish between electrons and protons (antiprotons).

In the maximum likelihood method, the energy deposit distributions in TRD are normalized and used as the probability distributions for each hit: $p^k(E_{dep})$. Then the signals from the 20 layers are combined to construct a likelihood $\mathcal{L}$ for each particle specie:

$$\mathcal{L} = \sqrt[n]{\sum_{k=1}^{n} P^k(E_{dep})} \tag{4.2}$$

For example, for electron and proton, $\mathcal{L}_e$ and $\mathcal{L}_p$ are constructed. According to Neyman-Pearson lemma [63] , the separation power can reach maximum in the form of the log-likelihood ratio. Therefore, the TRD estimator is defined as:

$$\Lambda_{TRD} = -\log(\frac{\mathcal{L}_{\mathrm{A}}}{\mathcal{L}_{\mathrm{A}} + \mathcal{L}_{\mathrm{B}}}) \tag{4.3}$$

If A = electron and B = proton, then the likelihood is called *TRDLikelihood*, which provides separation power for electron and proton. In figure 4.3, the TRD estimators for electron and proton are shown. The two kinds of particles can be very well separated in this estimator, as shown in this figure.

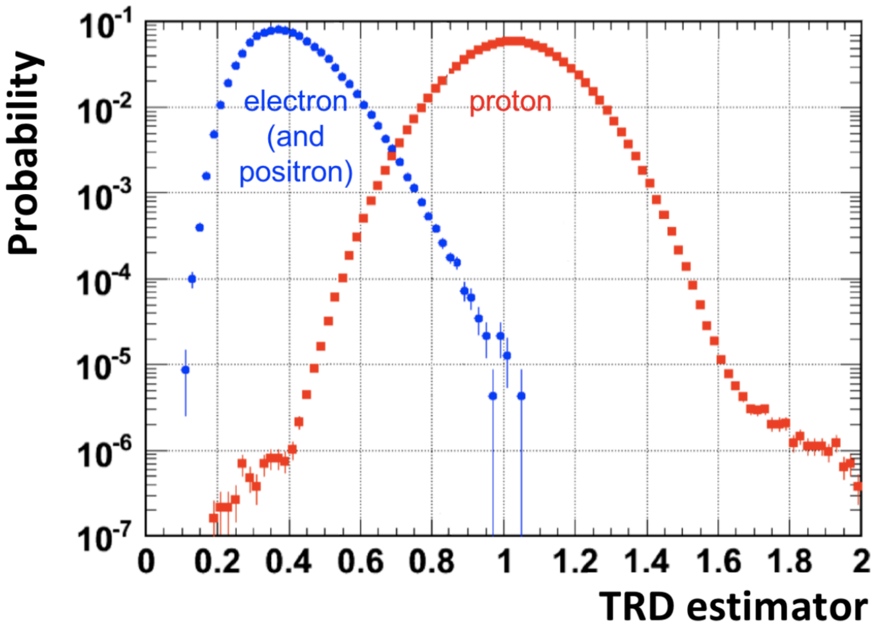

Figure 4.3: Seperation between the electrons and protons in TRDLikelihood estimator. [58]

4.4. Template Fit

In this section, the template fits are shown in detail for time averaged analysis and time dependent analysis respectively. For different rigidity ranges, the template fits are different due to sub-detector resolutions and background contributions. The selections used to get the signal and background templates will be discussed, and then the template fit result will be shown. In time dependent analysis, the template fit and the result in six Bartels Rotations will be given.

4.4.1. Time averaged analysis

The first ingredient to construct the antiproton to proton flux ratio is the event number. Due to the background level is not ignorable, cut-based analysis is not enough to get clean signals. Therefore, to get the clean signals, the template fit method is needed in this analysis to extract antiproton signals.

In different rigidity ranges, the detector resolutions and background components are different. The whole analysis is divided into three independent parts: low rigidity range (1.0 GV to 6.5 GV), intermediate rigidity range (3.0 to 19.5 GV), and high rigidity range (14.1 to 525 GV). The ranges are used as the same as the one in the previous AMS-02 antiproton analysis [50] . In each range, a dedicated template fit method is used to get antiproton signals.

Low Rigidity Range

In the low rigidity range, most backgrounds are electrons and interaction secondary particles like pions. The TOF beta can be used to separate antiprotons and backgrounds because of the different velocities of light particles and antiprotons in the low rigidity range. With the rigidity going up, the separation power from TOF beta decrease, and at the same time, the TRD separation power increase, so the TRDLikelihood can take over afterward in the intermediate rigidity range. A 2D temple fit in TRDLikelihood and TOF beta is used in the low rigidity range to have a smooth and stable separation power. The range in low rigidity is from 1.0 GV to 6.5 GV. The lower limit is due to the low statistics after the geometrical cutoff, and the higher limit is due to TOF beta resolution.

After cuts and selections, there are three major components in the data: antiprotons, electrons, and secondaries. The three templates must be constructed first to do the template fit. The antiproton template is taken from ISS positive rigidity data since the clean proton data is easy to extract from it, and the rigidity sign does not impact the absolute value of TOF beta and TRDLikelihood. The electron and the secondaries templates are taken from the ISS negative rigidity data. To get the clean electron and secondaries from it, dedicated selections should be applied respectively. Furthermore, after the preselection and selection introduced in section 4.1, the negative rigidity data to be fitted should be selected dedicatedly in the low rigidity range. In table 4.4 the full list of selections is shown.

In the table of 4.4, most cuts and selections are set with fixed value, while the TOFBetaCut: $\beta_{low}(R) < \frac{1}{\beta} - \frac{1}{\sqrt{(R^2)/(m_p^2+R^2)}} < 0.3$, and TRDLikelihoodCut: $\Lambda_{\mathrm{low}}(\mathrm{R}) <$ TRDLogLikelihood $<$ 1.7 are not. These two cuts are the template fit ranges, and the lower edge is rigidity-dependent. By varying the lower edge of the template fit range, the systematic uncertainty of the template fit can be evaluated. This will be discussed further later in section 4.10. For the representative result, the template fit is performed at 90% signal efficiency. The rigidity dependent lower edges are shown in figure 4.4.

Table 4.4: List of selections for templates

Antiproton template	**Electron Template**
TOFBetaCut	TOFBetaCut
TRDLikelihoodCut	TRDLikelihoodCut
$\mathrm{TRDLikelihood}_{\mathrm{P/He}} < 0.1$	β_{RICH} in RichAgl
TRDVTracksSize=1	$\beta_{RICH} - \frac{-R}{\sqrt{m_e^2+R^2}} > -0.002$
TRDNumberOfHits<40	TRDSegmentsXZ=1
	TRDSegmentsYZ=1
	TRDNumberOfHits<35

Secondaries Template	**Data Selection**
TOFBetaCut	TOFBetaCut
TRDLikelihoodCut	TRDLikelihoodCut
β_{RICH} in RichAgl	$\mathrm{TRDLikelihood}_{\mathrm{P/He}} < 0.1$
$\lvert\beta_{RICH} - \frac{-R}{\sqrt{m_\pi^2+R^2}}\rvert < 0.002$	TRDSegmentsXZ=1
TRDSegmentsXZ>1	TRDSegmentsYZ=1
TRDSegmentsYZ>1	
TRDNumberOfHits>50	

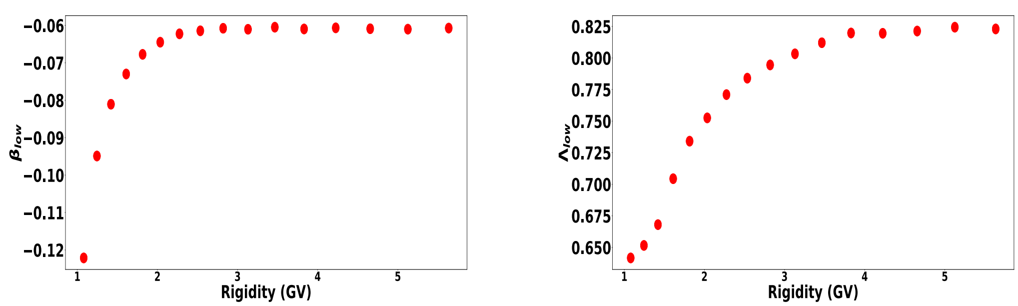

(a) (b)

Figure 4.4: The ridigity-dependent lower edge of template fit range for 90% signal efficiency. a). Lower edge for TOFBeta. b). Lower edge for TRDLikelihood.

In figure 4.5, the two projections of an example template fit in 3.64-4.02 GV are shown. The three templates are interaction secondaries, electrons, and antiproton signals.

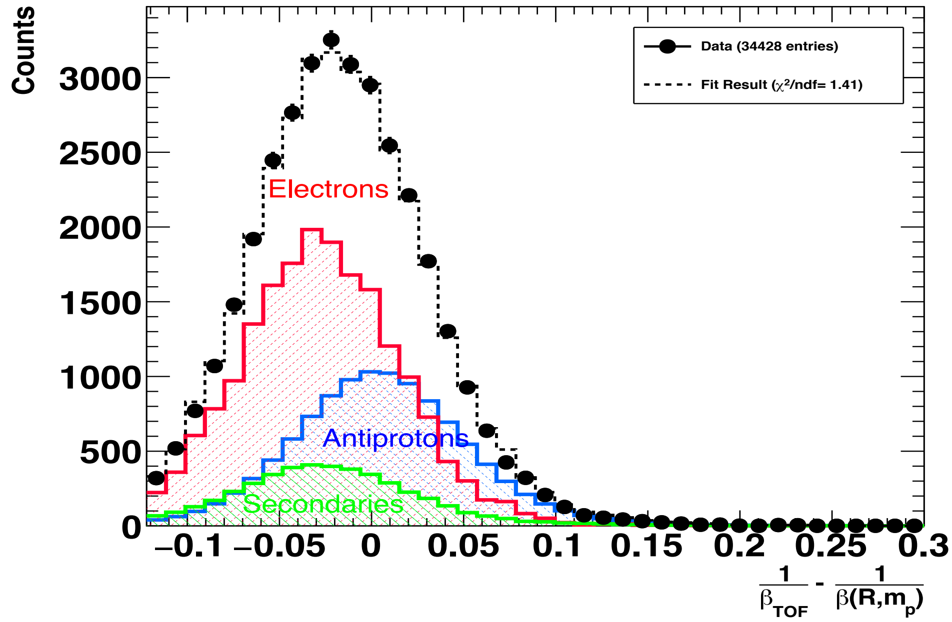

(a)

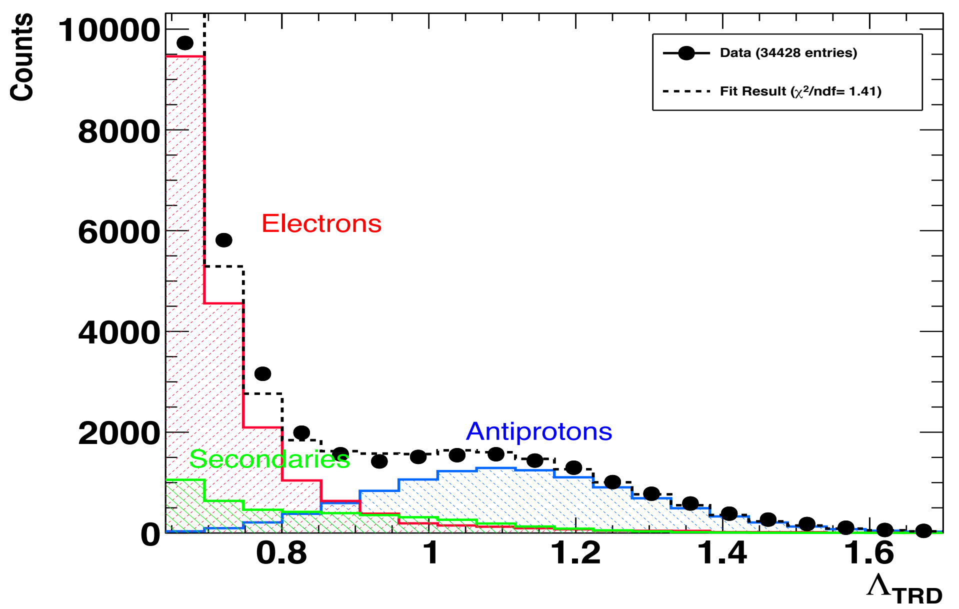

(b)

Figure 4.5: Example template fit in 3.64 to 4.02 GV in low rigidity range. a). 1/TOFBeta projection. In this projection, the value is subtracted by the 1/Beta with the assumption of antiproton mass, so the distribution can be normalized to be around 0. b).TRDLikelihood projection

The fit result gives the antiproton numbers in the low rigidity range. In figure 4.6 the antiproton number obtained is given. The Chi2/dof of the correspondent template fit is given in figure 4.7.

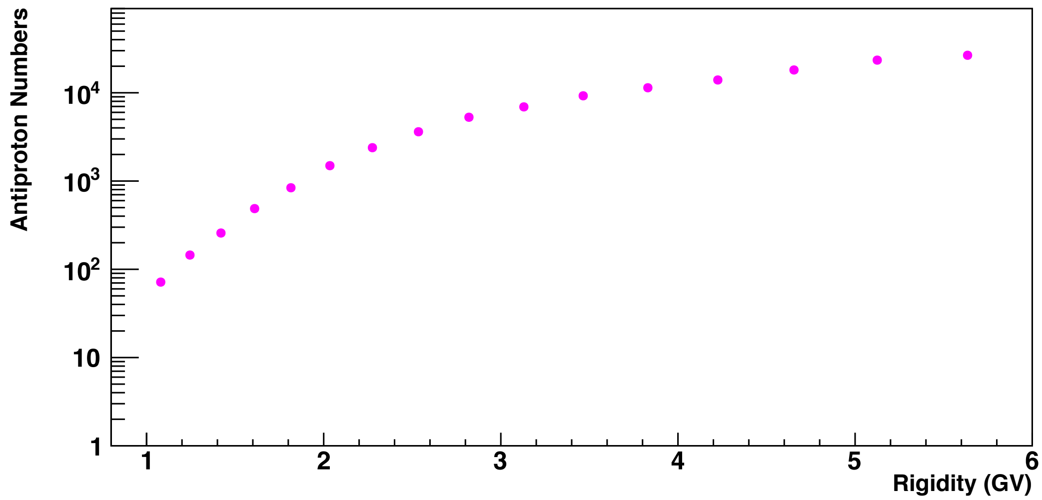

Figure 4.6: The antiproton numbers obtained from the template fit in low rigidity range

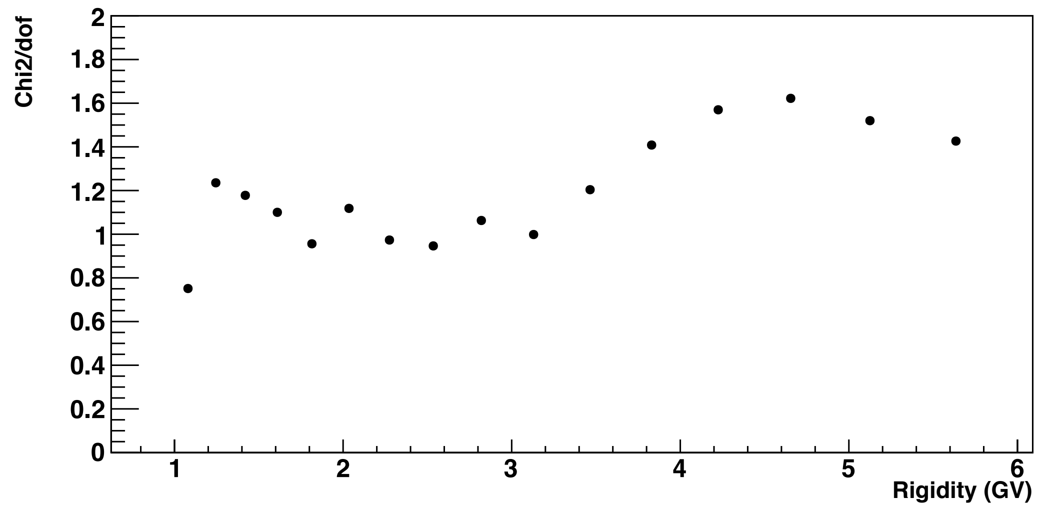

Figure 4.7: The Chi2/dof of template fit in low rigidity range

Intermediate Rigidity Range

In the intermediate rigidity range, the TOF Beta and TRDLikelihood 2D template fit is replaced by a 1D template fit in TRDLikelihood since the separation power of TOF Beta decreases with the rigidity going up and provides little power in this rigidity range. Above 20 GV, the component of charge confused protons gradually increases, so it has to be added as an additional template. Therefore the 1D template fit can only be implemented up to around 20 GV.

In the intermediate rigidity range, the interaction secondaries component is ignorable. Therefore, the templates in this rigidity range are only antiprotons and electrons. Like the template fit in the low rigidity range, the templates are also taken from ISS data. The antiproton is taken from positive rigidity data, and the electron template is taken from negative rigidity data. The dedicated selections for data in the intermediate rigidity range are applied before the template fit. In table 4.5, the full list of selections to get templates and data selections is given. The TRDLikelihoodCut: $-2.0 < \Lambda_{TRD} < \Lambda_{high}(R)$ represents the template fit range, and the rigidity dependent $\Lambda_{high}(R)$ has the same absolute value as the lower edge in the low rigidity range but opposite sign. To avoid the light particle background, the RichBetaCut: $\beta_{RICH} < \beta_{high}(R)$ is also applied to restrict in signal range. The $\beta_{high}(R)$ is determined by 90% signal efficiency. The ECALBDT is a value trained with ECAL response variables to separate protons and electrons. By applying a cut of 0.5 on ECALBDT, a clean electron sample can be obtained.

Table 4.5: List of selections for templates

Antiproton template	**Electron Template**	**Data Selection**
TRDLikelihoodCut	TRDLikelihoodCut	TRDLikelihoodCut
RichBetaCut	TRDNumberOfHits<35	RichBetaCut
TRDSegmentsXZ=1	ECALBDT>0.5	TRDSegmentsXZ=1
TRDSegmentsYZ=1	TRDSegmentsXZ=1	TRDSegmentsYZ=1
	TRDSegmentsYZ=1	

In figure 4.8, an example template fit of 10.1-11 GV is shown. The antiproton signals can be separated well with electron backgrounds.

The obtained antiproton number from the template fit is shown in figure 4.9. The correspondent Chi2/dof in intermediate rigidity range is given in 4.10.

High Rigidity Range

In the high rigidity range, the contribution of charge confusion protons increases with the rigidity going up. Therefore, the charge confusion estimator trained in section 4.2 should be used to separate antiprotons and charge confused protons. For electron separation, the TRD provides separation power, like in the low and intermediate rigidity range. In summary, a 2D template fit in charge confusion estimator and TRDLikelihood estimator is performed in this range to get the antiproton signal.

In the 2D template fit, the three templates are antiprotons, electrons, and charge confused

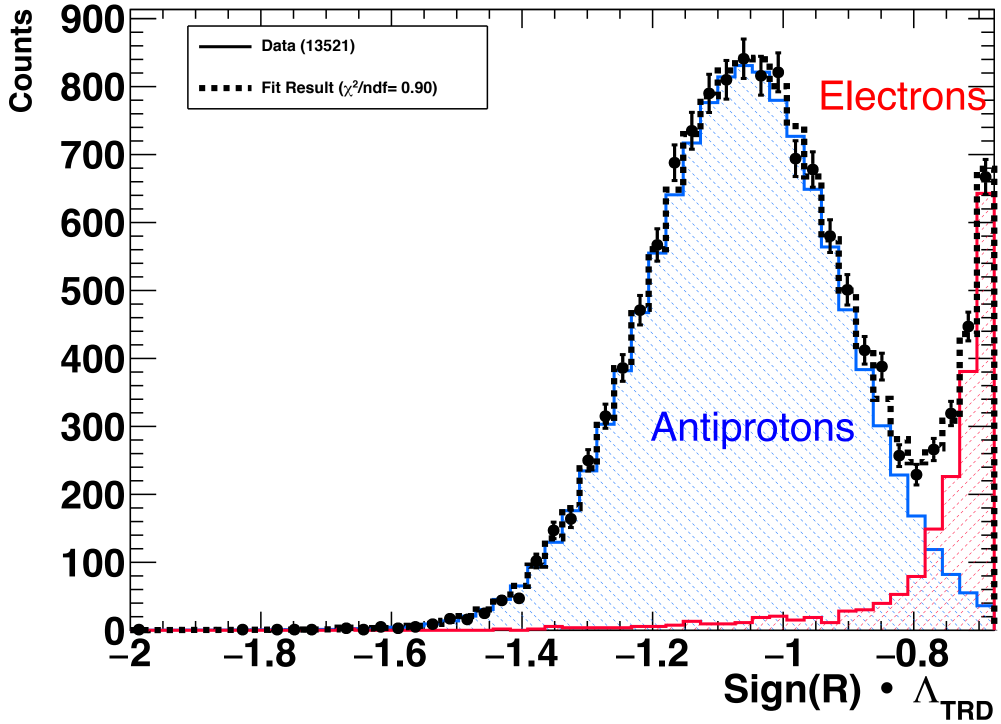

Figure 4.8: Example template fit in 10.1 to 11 GV in intermediate rigidity range

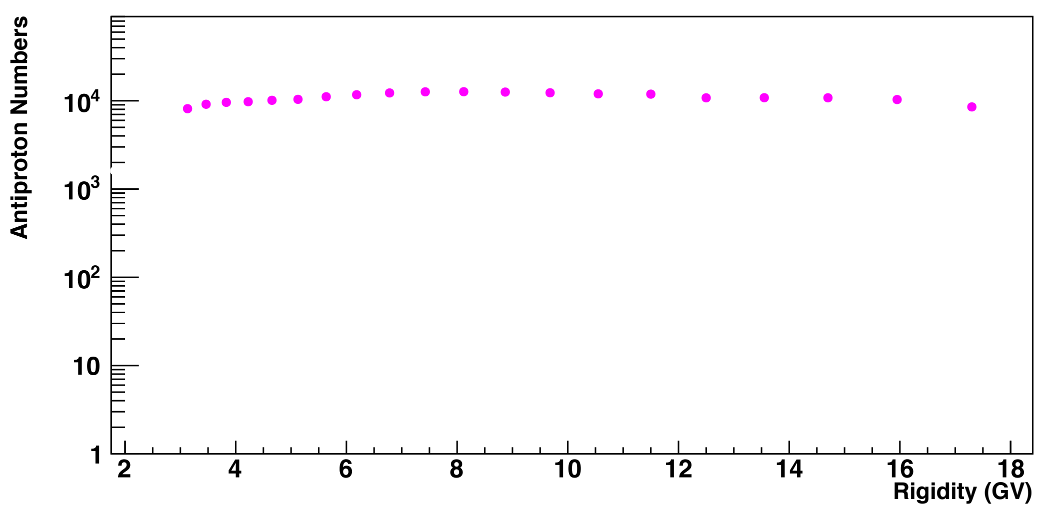

Figure 4.9: The antiproton numbers obtained from the template fit in intermediate rigidity range

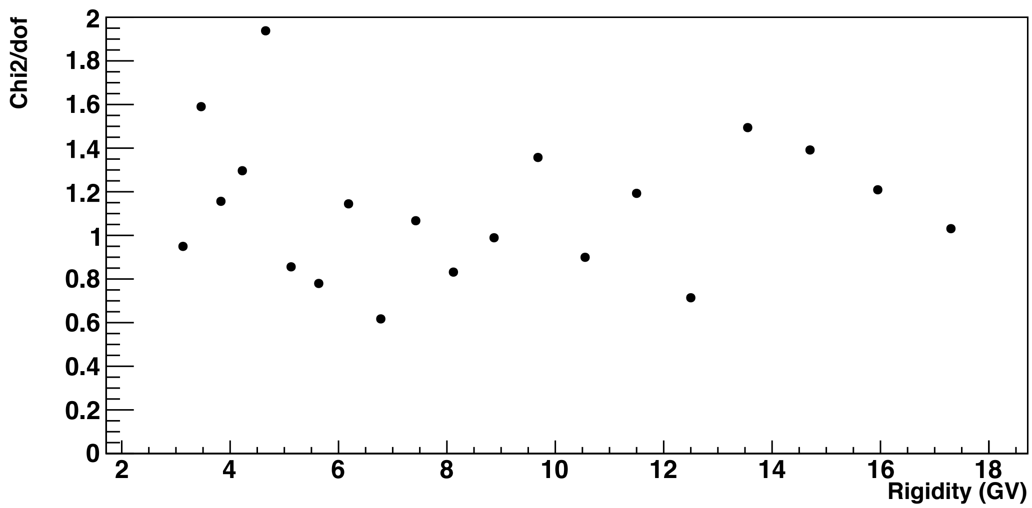

Figure 4.10: The Chi2/dof of template fit in intermediate rigidity range

protons. The antiproton template is taken from ISS positive rigidity data, and the electron template is taken from ISS negative rigidity data by selecting $0 <$ ECALBDT, the charge confused proton is taken from proton MC simulation by selecting negative rigidity. To avoid the contamination of Helium, the $\mathrm{TRDLikelihood}_{\mathrm{P/He}} < 0.3$ cut is applied for the negative rigidity data before template fit.

In figure 4.11, an example template fit in 175-211 GV is shown. To illustrate the separation, the 2D template fit is shown in two projections. In the charge confusion estimator projection, the antiproton and charge confusion protons can be separated. In the TRDLikelihood projection, the antiproton and electron can be separated.

The antiproton got from the 2D template fit in the high rigidity range is given in figure 4.12. The correspondent Chi2/dof is given in 4.13.

Once the template fits in the three rigidity range is done, the antiproton numbers from 1.0 to 525 GV can be obtained. In total, 481959 antiprotons are determined in this analysis.

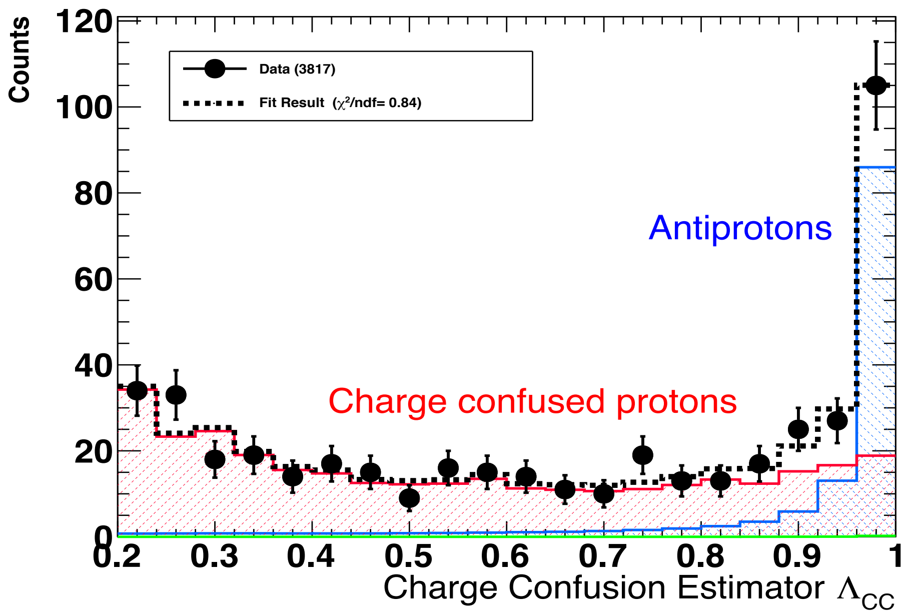

(a)

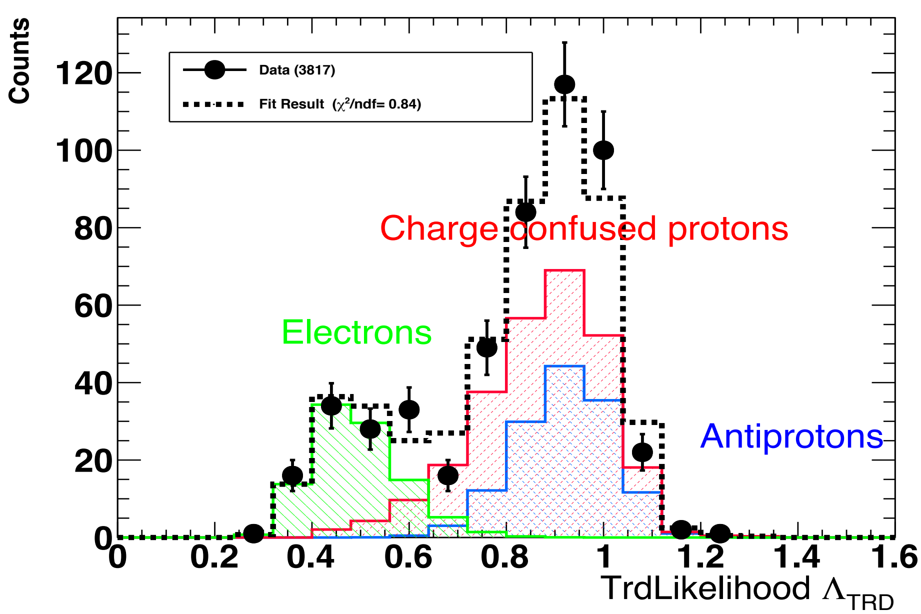

(b)

Figure 4.11: Example template fit in 175 to 211 GV in high rigidity range. a). The charge confusion estimator projection b). The TRDLikelihood projection

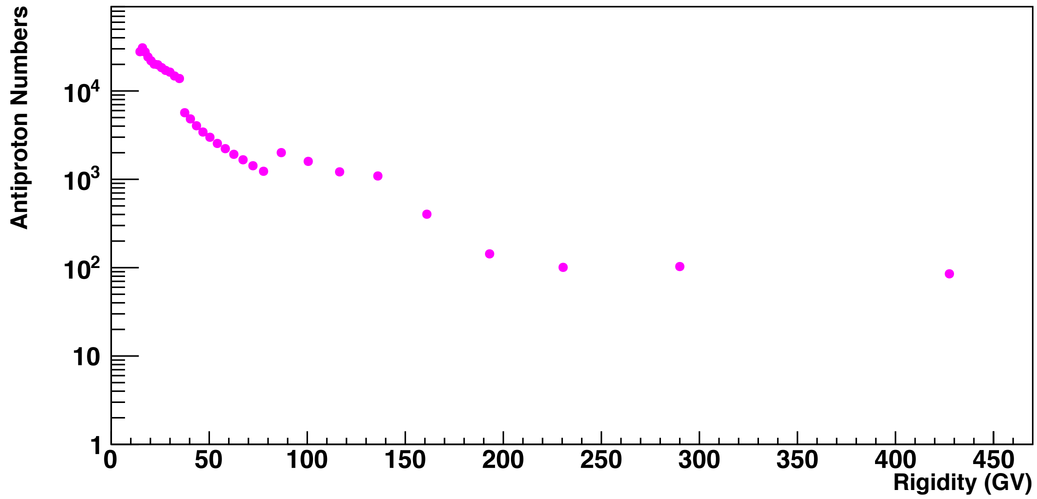

Figure 4.12: The antiproton numbers obtained from the template fit in the high rigidity range. The fluctuation is due to either merged rigidity bins width or usage of different tracker patterns.

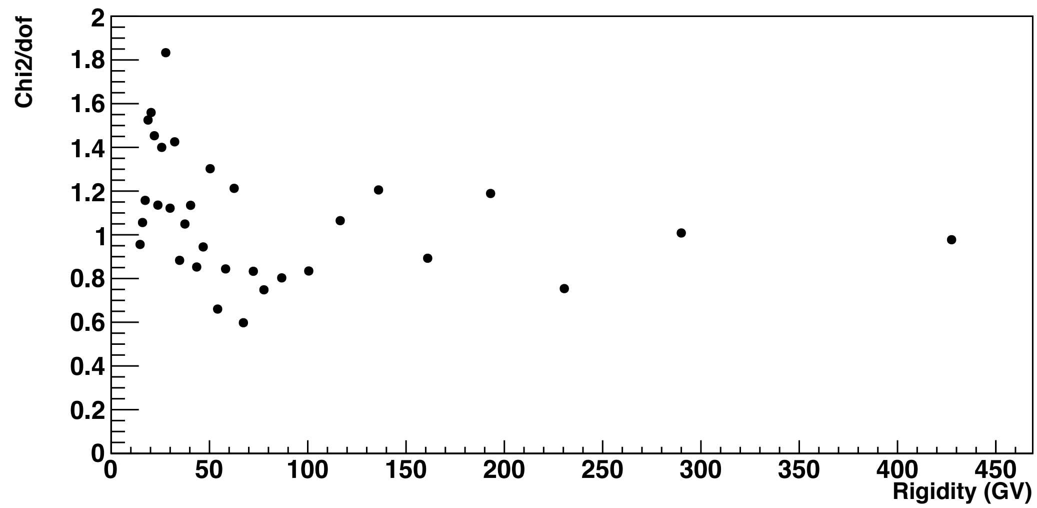

Figure 4.13: The Chi2/dof of template fit in high rigidity range

4.4.2. Time dependent analysis

For the time dependent analysis, the template fit strategy is the same as the one used in the time averaged analysis. The data is divided into every six Bartels Rotations bin. In each time bin, a template fit is performed to get the antiproton to proton ratio. Due to the limited statistics in each time bin, the rigidity bin is merged in every two original bins to increase the statistics.

The template selections are the same as the ones used in time averaged analysis. The only difference is the template fit range. To increase the statistics, the signal efficiency is increased from 90% to 95% in the low rigidity range and from 90% to 98% in the intermediate rigidity range.

A example template fit in 6.47 to 7.76 GV is given in figure 4.14. The fitted data is six Bartels Rotations data taken from Jan.07.2020 to June.17.2020.

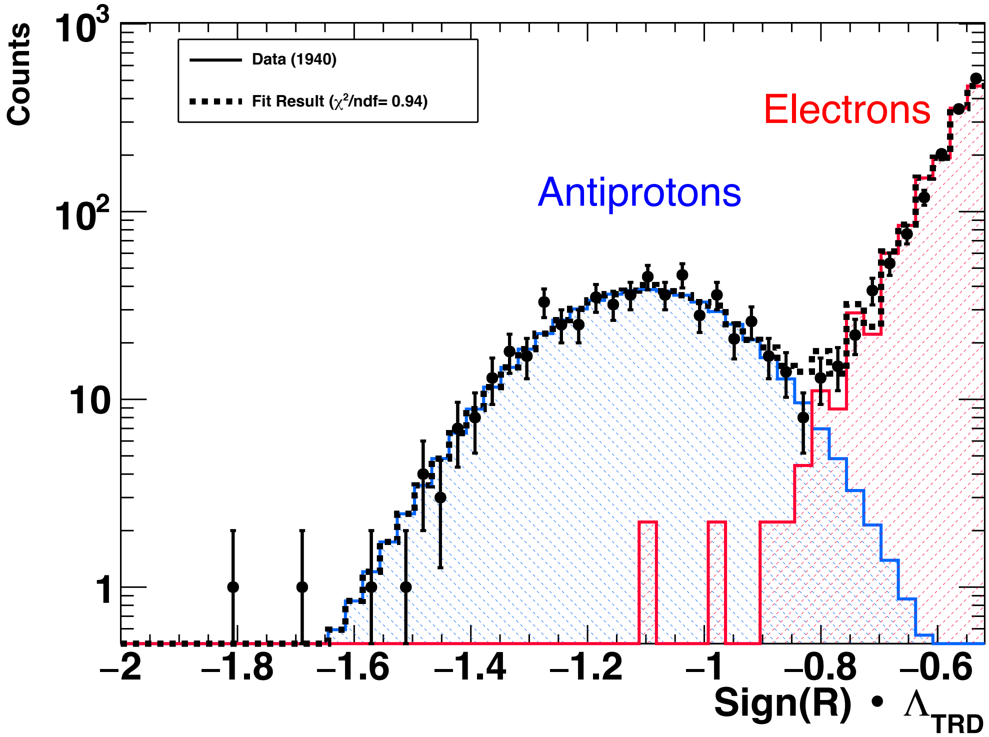

Figure 4.14: Example template fit in 6.47 to 7.76 GV with data collected Jan.07.2020 to June.17.2020.

The obtained antiproton numbers from the 23 six Bartel's Rotation's data is shown in figure 4.15. The correspondent Chi2/dof is given in figure 4.16.

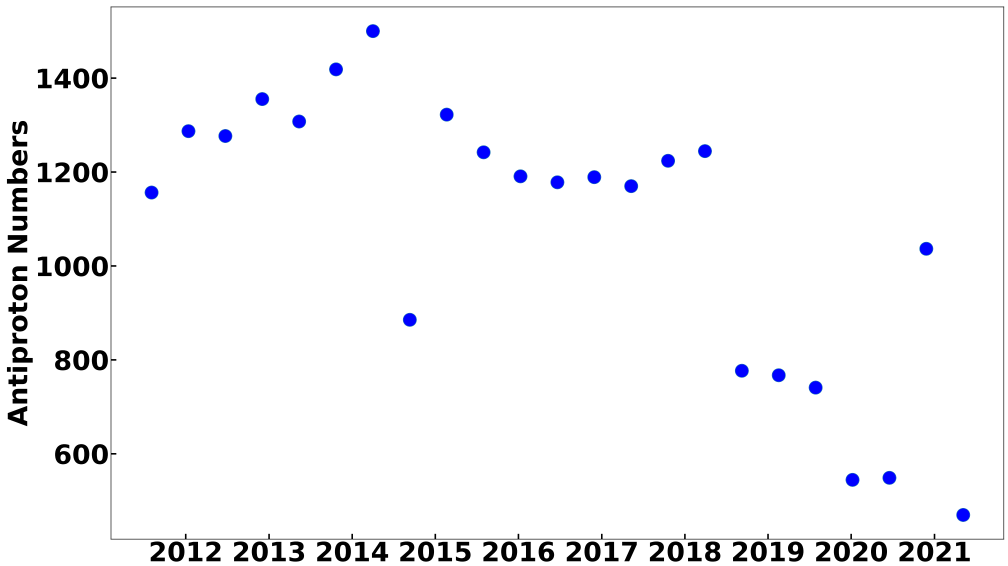

Figure 4.15: Antiproton numbers from template fit results in 6.47 to 7.76 GV with six Bartel's Rotation time resolution

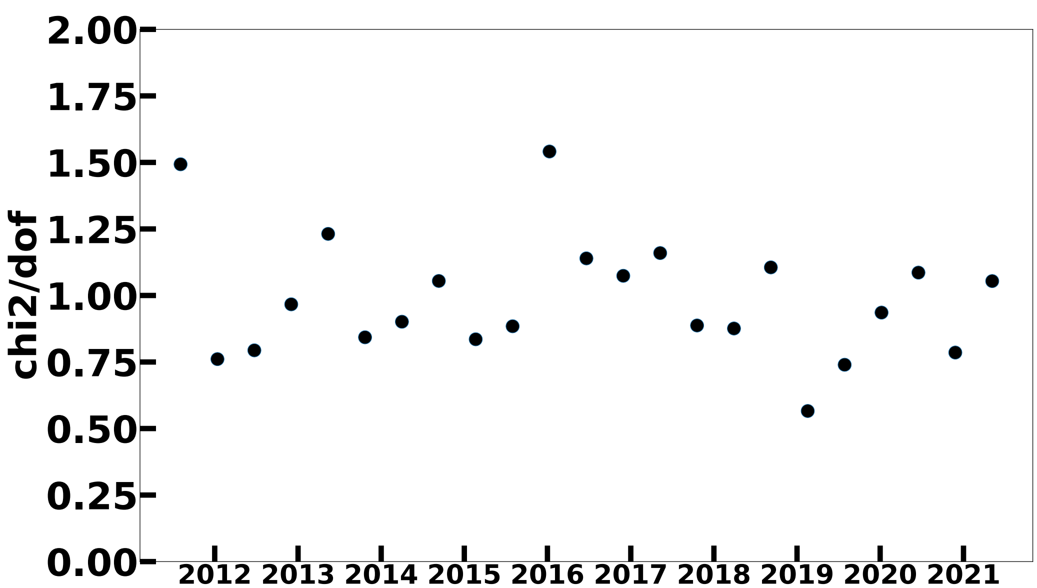

Figure 4.16: Chi2/dof of the template fits in 6.47 to 7.76 GV with six Bartel's Rotation time resolution

4.5. Effective Acceptance

After the event count is determined by template fit, the next important ingredient is effective acceptance.

For a spectrometer, the counting rate of a given specie particle depends on the flux intensity and the gathering factor, namely geometrical acceptance [96] . The geometrical acceptance is a fixed value for a fixed apparatus, but this assumes no interaction between the traversing particles and the apparatus. While for data analysis, dedicated cuts and selections should be applied. Therefore, considering this, the geometrical acceptance should be multiplied by the efficiencies of the cuts and selections. The product is called effective acceptance. See the equation 4.4. The larger the effective acceptance is, the more events can be collected.

$$A_{eff} = A_{geo} \times \epsilon_{cut} \tag{4.4}$$

Calculating the acceptance directly is not easy. The more practical way is to use the MC simulation method. In the AMS-02 experiment, extensive MC models with the help of Geant4 are widely used. The models assume that the whole detector is located in a cube with an edge length of 3.9 m. Above the top surface, a hypothetical flux source $S_{generate}$ is continuously emitting particles. These artificial particles are generated from this top plane and randomly go down through the whole detector.

According to [96] , the acceptance can be calculated with two ingredients: the number of triggered events $N_{triggered}$ and the number of generated events above the top plane $N_{generate}$. The formula is given in equation 4.5. For the calculation of geometrical acceptance, it can be achieved without applying any cuts and selections, and the triggered events can only be determined by the geometry of the detectors. For the calculation of effective acceptance, apart from the geometry of the detectors, the cut efficiency also reduces the number of triggered events.

$$A_{eff} = \pi \cdot A \cdot \frac{N_{triggered}(R_{true})}{N_{generate}(R_{true})} \tag{4.5}$$

where $A = 3.9m \cdot 3.9m$.

The antiproton and proton effective acceptance is taken from MC. Due to the small difference in passing efficiency between ISS data and MC, the effective acceptance from MC needs to be corrected with the Data/MC efficiency ratio. For flux analysis, this has to be done with the "Tag and Probe" method.

For antiproton to proton flux ratio analysis, the effective acceptance ratio is not equal to one because of the differences in cross sections between antiproton and proton. The effective acceptance ratio is rigidity dependent. While for the proton and antiproton effective acceptances, both of them should apply a data/MC correction, and this correction can strictly be canceled out. See equation 4.6. The way to deal with it is the same as the one used in positron/electron ratio analysis in [97] . Therefore, the effective acceptance ratio is purely determined by MC simulations.

$$\frac{A_p}{A_{\bar{p}}} = \frac{A_p^{MC}}{A_{\bar{p}}^{MC}} \cdot \frac{1+\delta_p}{1+\delta_{\bar{p}}} = \frac{A_p^{MC}}{A_{\bar{p}}^{MC}} \tag{4.6}$$

In figure 4.17, the antiproton to proton effective acceptance ratio is shown. In different rigidity ranges, the selections are slightly different. Therefore the effective acceptance ratios are also determined individually.

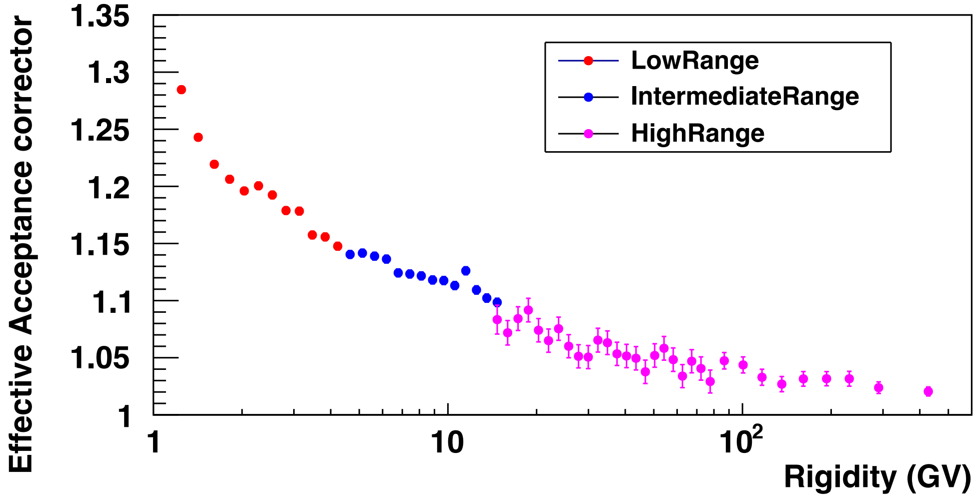

Figure 4.17: Proton to antiproton effective acceptance ratio in three rigidity ranges.

4.6. Measuring Time

To construct the flux, the next ingredient is measuring time. The measuring time is the total time that all the sub-detectors are in nominal operation and could record events. Due to the detector's operation cuts and the trigger dead time, the measuring time is lower than the exposure time, which is the total data-taking time when the experiment is running.

Because of the trigger dead time, if the event trigger rate goes up and surpasses the threshold, then not all the events can be fired and recorded. This leads to a ratio of recorded events over all events, called live time fraction. Because the amount of incoming particles depends on the ISS position in the geomagnetic field, the live time fraction is close to one in most areas but less than one in high latitude areas, see 4.18. Also, in SAA, there are plenty of low energy particles going through. Therefore, the trigger rate in this area is very high, and the live time fraction is very low correspondently. For the entire data-taking period, the live time fraction is mostly above 90%. In figure 4.20, the trigger vs. particles per trigger is presented. For most triggers, the number of analysis particles per trigger is around 0.11.

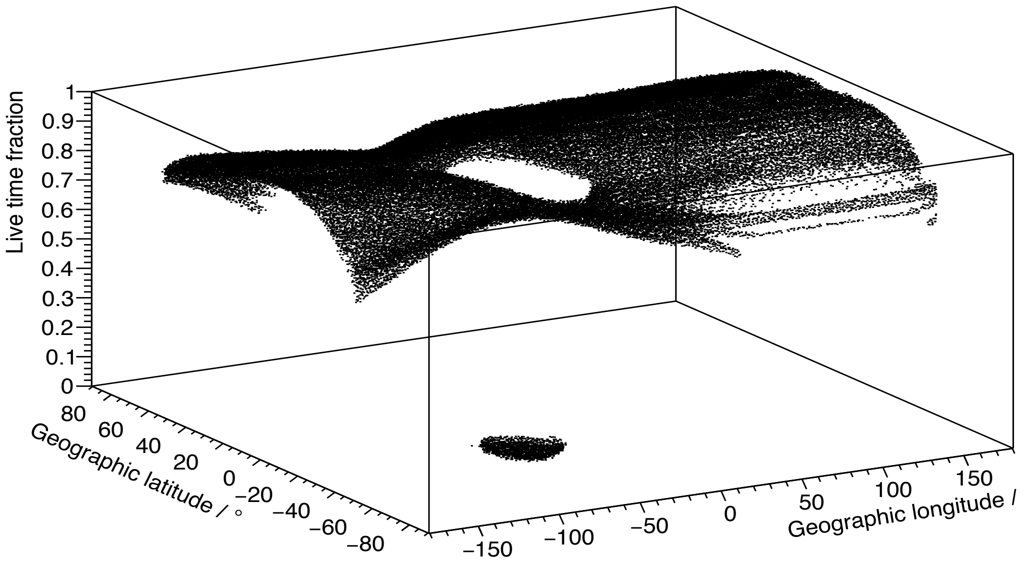

Figure 4.18: Live time fraction vs. ISS position. The live time fraction in most area is above 0.9 while in SAA is extremely low.

Due to the earth's magnetic field, the charged particle can be deflected before it reaches the detectors at Low Earth Orbit (LEO), where the AMS-02 is located. The deflection power depends on the particle's rigidity and the particle's relative location to the magnetic field line.

The earth's magnetic field is roughly tilted at 11° with respect to the earth's rotation axis, as illustrated in figure 4.21. Therefore, the lowest rigidity threshold to penetrate the earth's magnetic field should be a function of the earth's location. The lowest rigidity threshold is called *rigidity cutoff*.

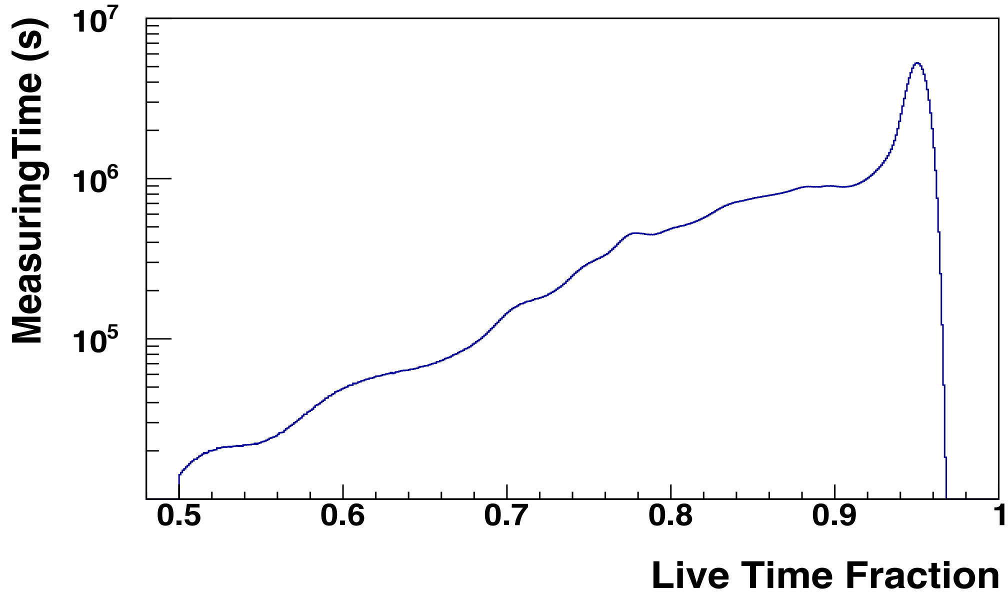

Figure 4.19: Measuring time as a function of live time fraction. In most of the measuring time, the live time fraction is above 0.9.

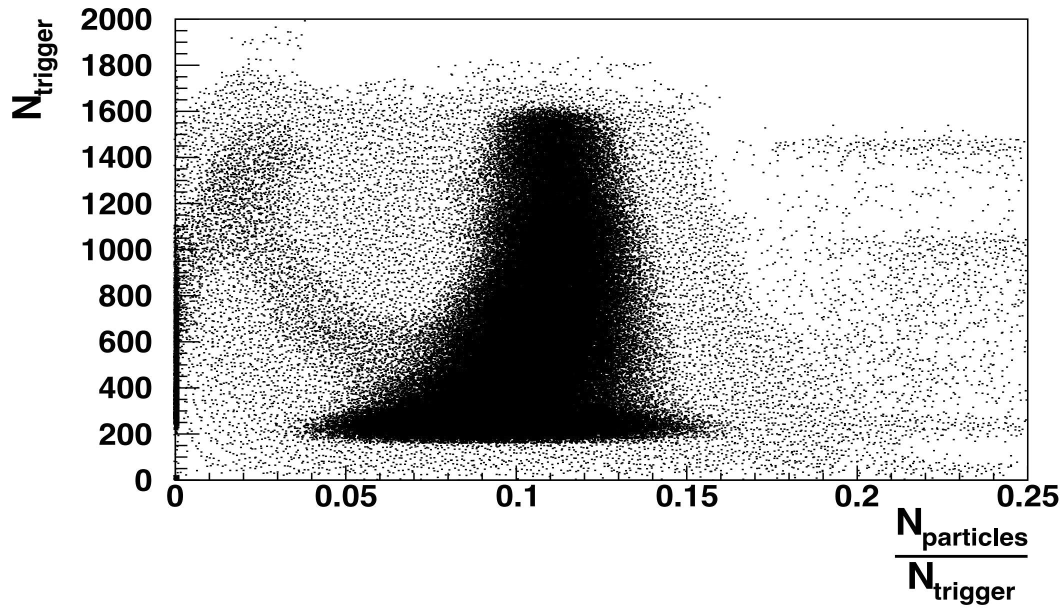

Figure 4.20: Triggers as a function of particle over trigger ratio. For most triggers, each trigger fires around 0.11 particles

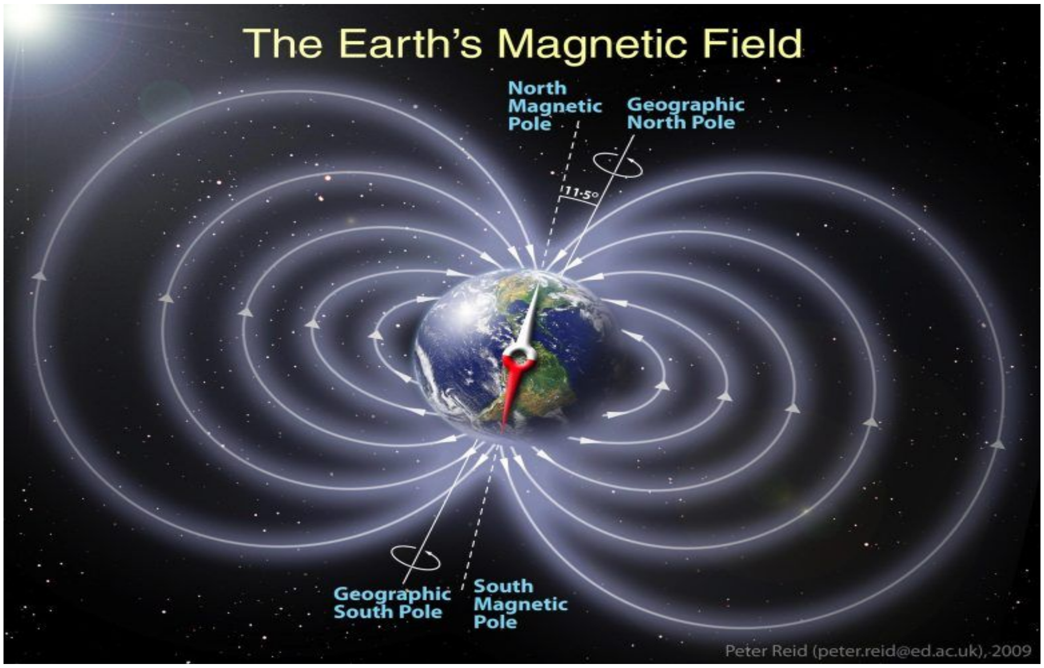

Figure 4.21: Illustration of Earth's magnetic field. Credit: Peter Reid, The University of Edinburgh

To calculate the rigidity cutoff, there are two methods used in AMS-02 collaboration. The first one is the Størmer cutoff, the equation 4.7 gives the way to calculate the Størmer rigidity cutoff R_c [98] :

$$R_c = \frac{M cos^4 \lambda}{r^2(1 + \sqrt{1 - \sin\epsilon \cdot \sin\delta \cdot \cos^3\lambda})^2} \tag{4.7}$$

where M is the geomagnetic dipole moment, λ is the magnetic latitude, r is the altitude distance from the dipole center, ϵ and δ are the zenith angle and azimuthal angle, respectively.

With the cuts and selection introduced in section 4.1, the calculated Størmer rigidity cutoff as function of ISS position is given in figure 4.22.

The total measuring time can be obtained by integrating the live time fraction in every second of the whole data-taking period. With the preselection about sub-detector operation quality introduced in section 4.1, the resulting measuring time used in this analysis is shown in figure 4.23. The integrated data-taking time from 20. May 2011 to 03. May 2021 is 3636 days. Because of the ISS orientation, detectors operation like TRD gas refills or in the SAA, the actual measuring time is around 68% of the total data taking time. This leads to a measuring time of 2488 days.

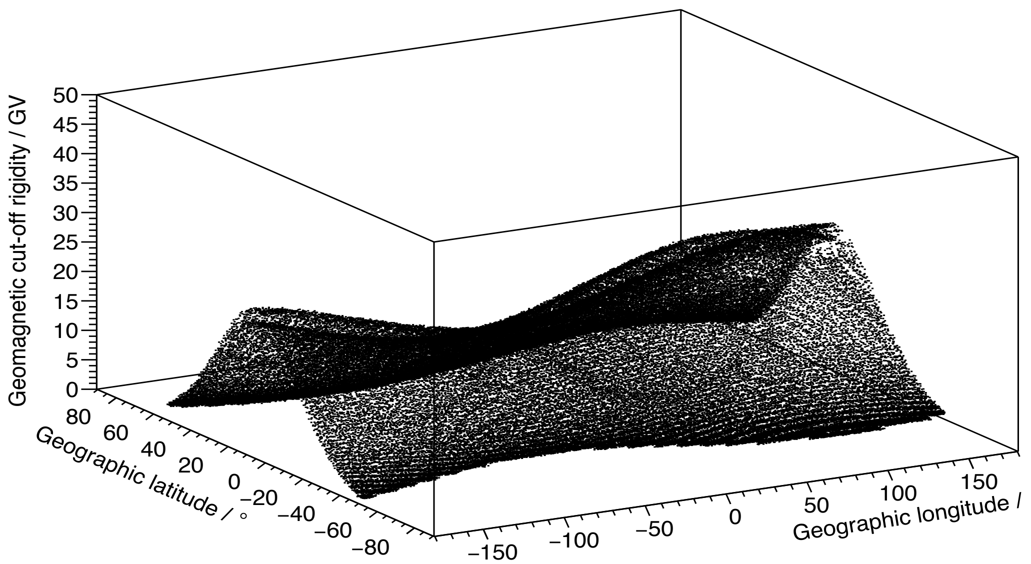

Figure 4.22: The Størmer rigidity cutoff used in this analysis as a function of ISS Position. The maximum of the cutoff is less than 30 GV.

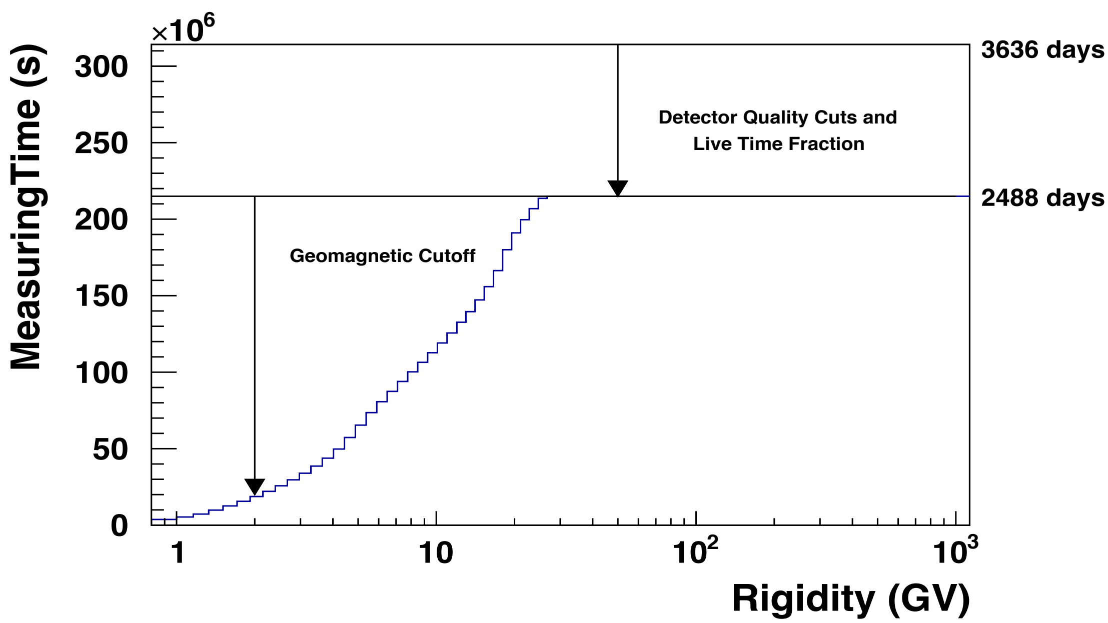

Figure 4.23: The measuring time obtained from the Størmer geomagnetic cutoff. After the quality cuts and live time fraction, the resulting total measuring time is around 2488 days.

Another method used in AMS-02 collaboration to calculate the rigidity cutoff is the IGRF method. To calculate the particle penetrating the magnetic field, a solution is to consider the backtracing particles. If all the backtracing particles from a certain position and rigidity are primary particles, namely from outer space, the rigidity is the cutoff rigidity for this position. The magnetic field model should be determined first in this numerical calculation of backtracing particles. One model option is the International Geomagnetic Reference Field (IGRF) model. Therefore, the name for calculating the rigidity cutoff is called IGRF method.

Figure 4.24 shows the comparison between the measuring time achieved from the IGRF method and the Størmer cutoff method. As shown in the figure, compared to the IGRF method, using the Størmer cutoff leads to higher statistics in the low rigidity range. This is important for time dependent analysis since the statistics in the fine time bin are limited. Also, using the IGRF method leads to almost zero measuring time in the first one to two rigidity bins. Therefore, the data could only be analyzed in higher rigidity bins. So in this analysis, the Størmer rigidity cutoff is used to determine the measuring time.

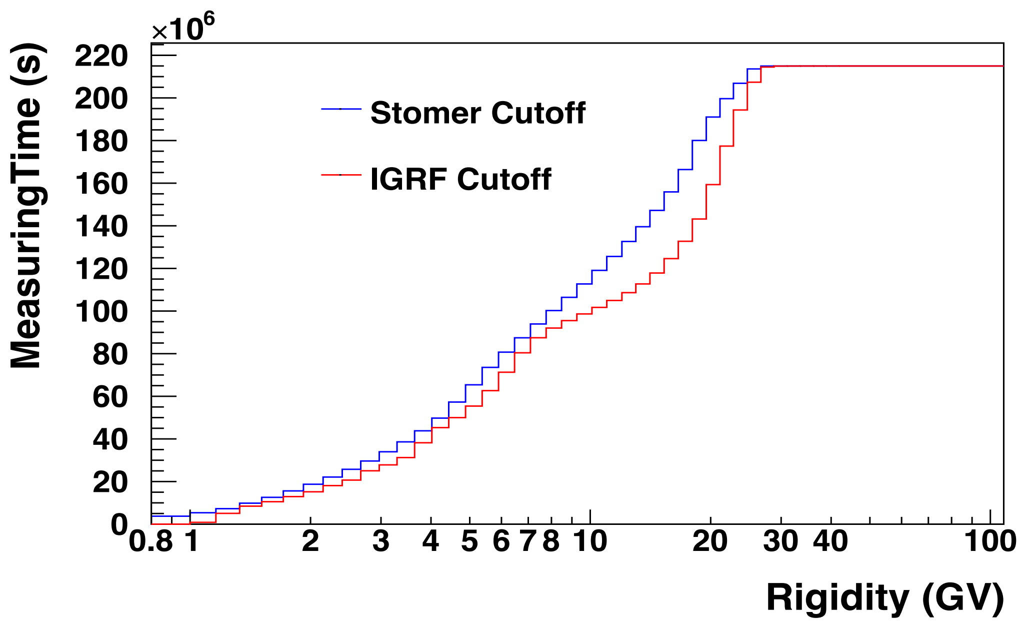

Figure 4.24: The comparison between the Størmer and IGRF cutoffs. The IGRF cutoff leads to lower measuring time

4.7. Trigger Efficiency

After the measuring time, the next ingredient to construct flux is trigger efficiency.

The trigger efficiency is the triggered events over the total events when the particles go through the detectors. In the AMS-02 experiment, the trigger logic is based on the response of the TOF, the ACC, and the ECAL. There are three stages in AMS-02 trigger architecture: "Fast trigger", "Level 1 trigger", and "Level 3 trigger". The three stages are processed in sequence, namely the next stage is activated after the previous stage is fulfilled. Because the bandwidth is enough to transfer the data to the ground, the "Level 3 trigger" is not activated.

There are two kinds of "Fast trigger" [86] . The first one is using the TOF. If the FTC and FTZ trigger decisions (see definition in [89]) are fulfilled, the first kind of fast trigger is set. The second one is using the ECAL. This kind of trigger is generated by showers detected by the ECAL. The first and second fast triggers are for charged particles and photons respectively.

The "Layer 1 trigger" has seven kinds:

- Single charged: Has High Threshold signals (HT) in all four TOF layers, also no ACC hits.
- Fast ions: Has Super High Threshold (SHT) signals in all four TOF layers, also less than five ACC hits. (From 26 Feb 2016, the second condition changed to less than eight ACC hits to improve statistics.)
- Slow ions: Has SHT signals in all four TOF layers within 640 ns.
- Electrons: Has HT signals in all four TOF layers, also requires at least two ECAL superlayers signals in both XZ and YZ planes.
- Photons: Has an ECAL shower with less than 20 degree zenith angle in both XZ and YZ planes.
- Unbiased TOF: Has at least three out of four TOF layer HT signals. Prescaling to 1% in order to reduce the trigger rate and save bandwidth.
- Unbiased ECAL: Has signals in at least two ECAL superlayers in the X-Z or Y-Z plane. Prescaling to 0.1% to reduce the trigger rate and save bandwidth.

Among the seven kinds of Layer 1 triggers, the first five are called *physics trigger*. In this analysis, only the physics triggered events are used for counting the signal numbers. To construct the flux, the last two unbiased non-physics trigger are used to calculate the physics trigger efficiency.

Due to a technical issue in the trigger, the two unbiased triggers can be triggered at the same time, therefore the double-counting events should be corrected:

$$\frac{1}{f_{\text{both}}} = \frac{1}{f_{\text{TOF}}} + \frac{1}{f_{\text{ECAL}}} - \frac{1}{f_{\text{TOF}} \cdot f_{\text{ECAL}}} \tag{4.8}$$

where the f_{TOF}=100 is the Unbiased TOF prescaling factor and the f_{ECAL}=1000 is the Unbiased ECAL prescaling factor. So the $f_{\mathrm{both}} \approx 90.99$.

Once the prescaling factor is determined, the trigger efficiency can be calculated by comparing the number of physics trigger events and the unbiased non-physics trigger events:

$$\epsilon_{Trigger}(R) = \frac{N_{phys}(R)}{N_{phys}(R) + f_{tof} \cdot N_{tof}(R) + f_{ecal} \cdot N_{ecal}(R) + f_{tof+ecal} \cdot N_{tof+ecal}(R)} \quad (4.9)$$

In figure 4.25, the trigger efficiency of proton is shown as an example. For the antiproton, the trigger efficiency is assumed to be the same.

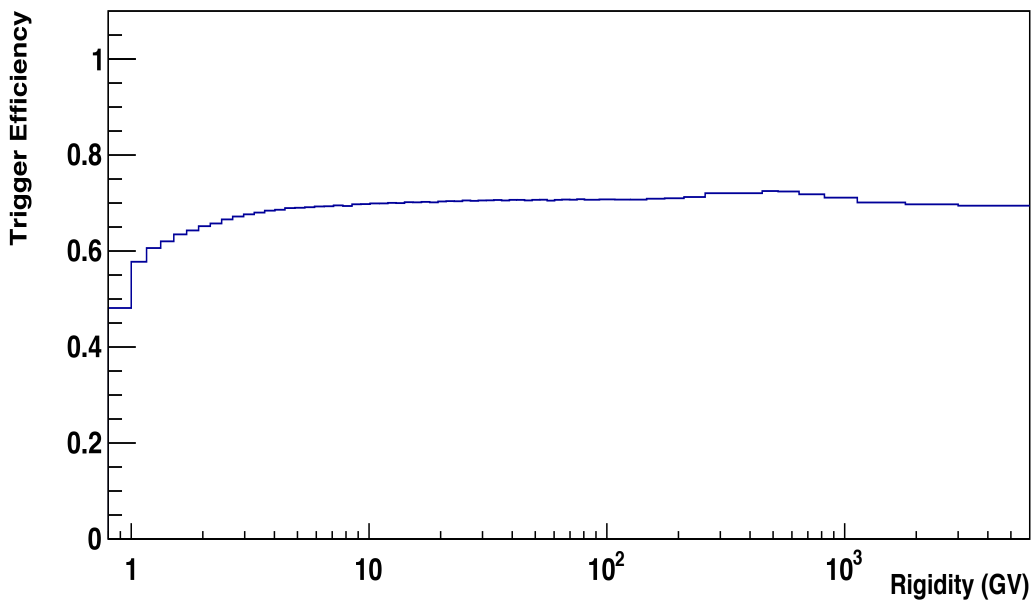

Figure 4.25: The proton trigger efficiency.

Since this analysis is only focused on antiproton to proton flux ratio, the trigger efficiency of proton ϵ_p and antiproton $\epsilon_{\overline{p}}$ should be strictly canceled out in calculation. However, trigger efficiency is still needed in the unfolding procedure in next section.

4.8. Unfolding

To calculate the flux, the number of events should be determined in true rigidity, which is the rigidity at the Top Of Instrument (TOI). However, the number of events from template fit is determined in reconstructed rigidity. There are some differences between these two rigidities because of the limited tracker resolution. Some events may end up in other rigidity bins, and this effect is called "bin to bin migration". To correct this effect, a procedure called *unfolding* should be applied.

There are many unfolding methods to estimate this effect. In this analysis, the "Bayesian unfolding" method is used. The "Bayesian unfolding" [99] is provided by the "RooUnfold" package in ROOT [100] , and the method is also used in AMS-02 electron and positron analysis [97] .

The unfolded count $\hat{n}$, namely the event count in the true rigidity, can be obtained by multiplying the raw event count n (the event count in reconstructed rigidity) and the unfolding matrix U:

$$\hat{n} = \mathrm{U} \cdot \mathrm{n} \tag{4.10}$$

A simple correction factor by matrix inversion is the easiest way to estimate the effect, but the process is not numerically stable. Therefore the unfolding matrix U in equation 4.10 is the unfolding matrix, which is calculated in the iteration process based on migration matrix M.

The migration matrix M contains the information about the "bin to bin migration" and can be taken from the MC simulation directly. The matrix is shown in a 2D histogram. The X axis is the reconstructed rigidity by the tracker, and the Y axis is the true generated rigidity simulated in the MC. In this analysis, the signals are determined with different selections for different rigidity ranges. Also, for the different tracker patterns, the migration matrices are different due to the different tracker pattern resolutions. In figure 4.26, the migration matrix of full span in high rigidity range is given as an example, which is taken from proton MC simulation. The histogram is normalized to unity for illustration. From the figure, the diagonal elements of the matrix are the events whose true rigidity matches the reconstructed rigidity, which is the dominant part of the total events. With the rigidity going up, the bin contents of non-diagonal elements are going up. This is due to the tracker resolution becoming worse in higher rigidity.

As introduced in the section 4.6, the collected data have applied the rigidity cutoff. This cutoff effect is not simulated in the MC simulation process, so it must be fixed before we use the migration matrix. To consider this, the shape of measuring time is used as a weight for the events under the rigidity cutoff.

In this analysis, the focus is the antiproton to proton ratio. Therefore, the unfolding process has to be done for antiproton raw numbers and proton raw numbers respectively. The antiproton raw numbers are taken from template fit results, and the proton raw numbers are the event numbers after the cuts and selections shown before. In figure 4.27, the residual of raw counts and unfolded counts in the high rigidity range is given. The overall correction effect is less than 10% in the unfolded ratio.

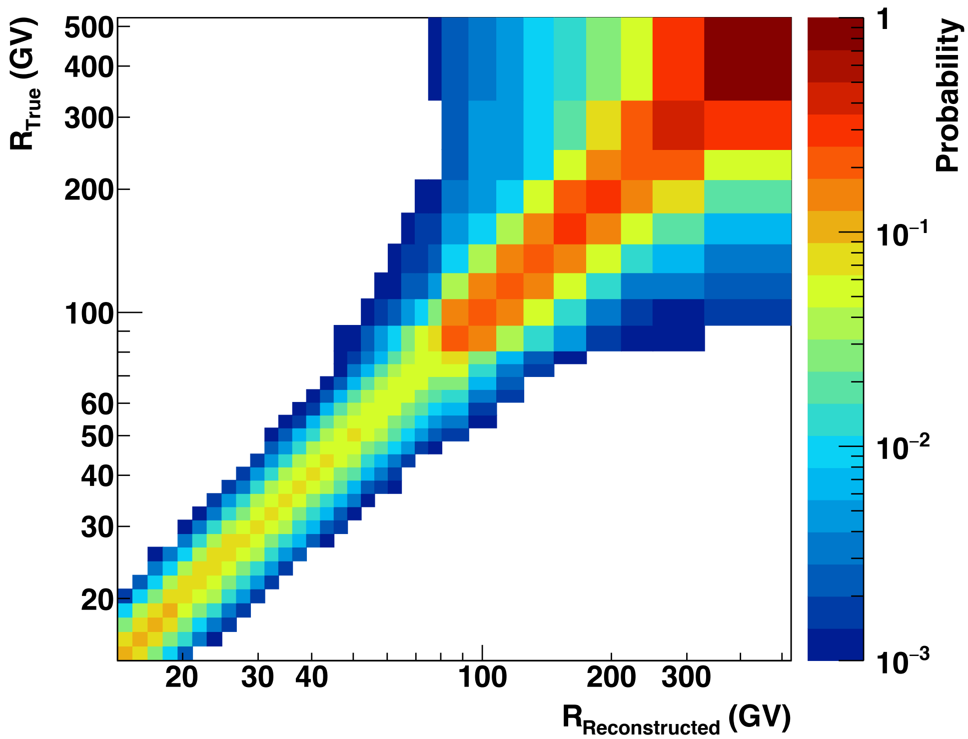

Figure 4.26: The migration matrix for full span in high rigidity range. The X axis is the reconstructed rigidity from the Tracker, the Y axis is the true rigidity from the generated momentum in MC.

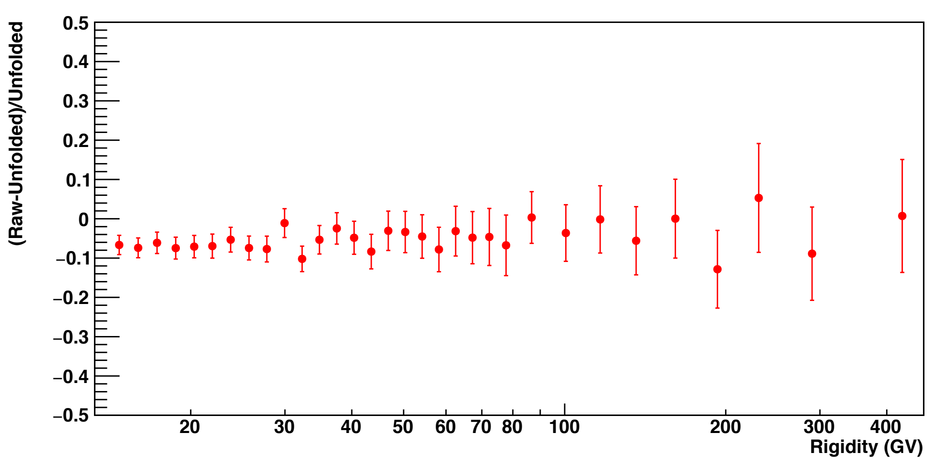

Figure 4.27: The residual over unfolded number for full span in high rigidity range

4.9. Antiproton To Proton Flux Ratio Calculation

In this section, the calculation of the antiproton to proton flux ratio is given.

This thesis focuses on the antiproton to proton flux ratio. Therefore the dedicated formula for antiproton to proton flux ratio should also be discussed in advance based on flux calculation equation 4.1. From previous sections in this chapter, all the ingredients have been shown already, so the antiproton to proton flux ratio can be calculated.

$$\begin{aligned}\Phi_{\bar{p}}(|R|) &= \frac{N_{\bar{p}}(|R|)}{\Delta R_{\bar{p}} \cdot T_{\bar{p}}(|R|) \cdot A_{\bar{p}}(|R|) \cdot \epsilon_{\bar{p}}(|R|)} \\ \Phi_{p}(|R|) &= \frac{N_{p}(|R|)}{\Delta R_{p} \cdot T_{p}(|R|) \cdot A_{p}(|R|) \cdot \epsilon_{p}(|R|)}\end{aligned} \tag{4.11}$$

By definition, the antiproton to proton flux ratio is the antiproton flux divided by the proton flux. In this process, some terms can be strictly canceled out, like the procedure of AMS-02 positron to electron flux ratio analysis in [97] . Therefore, the overall calculation can be simplified:

$$\begin{aligned}\frac{\Phi_{\bar{p}}(|R|)}{\Phi_{p}(|R|)} &= \frac{N_{\bar{p}}(|R|) \cdot \Delta R_{p} \cdot T_{p}(|R|) \cdot A_{p}(|R|) \cdot \epsilon_{p}(|R|)}{N_{p}(|R|) \cdot \Delta R_{\bar{p}} \cdot T_{\bar{p}}(|R|) \cdot A_{\bar{p}}(|R|) \cdot \epsilon_{\bar{p}}(|R|)} \\ &= \frac{N_{\bar{p}}(|R|)}{N_{p}(|R|)} \frac{A_{p}(|R|)}{A_{\bar{p}}(|R|)} \\ &= \frac{N_{\bar{p}}(|R|)}{N_{p}(|R|)} \frac{A_{p}^{MC}(|R|)}{A_{\bar{p}}^{MC}(|R|)} \frac{1+\delta_{p}(|R|)}{1+\delta_{\bar{p}}(|R|)} \\ &= \frac{N_{\bar{p}}(|R|)}{N_{p}(|R|)} \frac{A_{p}^{MC}(|R|)}{A_{\bar{p}}^{MC}(|R|)}\end{aligned} \tag{4.12}$$

From the dedicated equation 4.12 for antiproton to proton flux ratio, obviously some terms are canceled out like measuring time, trigger efficiency, rigidity bin width, and the data/MC corrections of effective acceptance. This gives many conveniences for calculation. Although the measuring time and trigger efficiency is canceled out in the ratio calculation, they are still used in the unfolding process.

The formula for the time dependent antiproton to proton flux ratio is the same. The only difference is the number of event is taken from individual template fit in every six Bartels Rotations bins.

4.10. Systematic Uncertainty

In this section, systematic uncertainty is discussed. Due to different template fit methods in three different rigidity ranges. The systematic uncertainty is discussed individually in three rigidity ranges.

The antiproton to proton flux ratio is calculated in equation 4.12. There are two components in this equation: Number of events N and effective acceptance A. Therefore, the sources of systematic uncertainty should also be considered from these two variables.

The first source of systematic uncertainty is effective acceptance. Since the effective acceptance data/MC correction is canceled out, so it is completely decided by the MC simulation. Due to the asymmetry of the interaction cross sections, the antiproton and proton effective acceptances impact the flux ratio. Therefore, two dedicated MCs are generated for antiproton and proton respectively to estimate the asymmetry of the interaction cross sections. In these two MCs, the interaction cross sections are varied with $\pm 10\%$ change. This transfers to systematic uncertainty from effective acceptance. In figure 4.28, the obtained systematic error is shown.

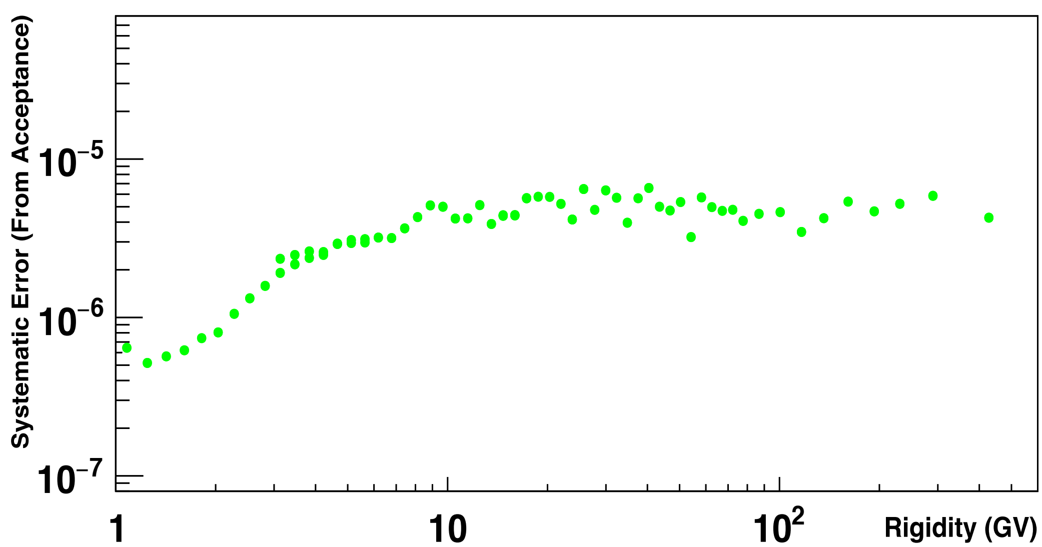

Figure 4.28: The systematic error from acceptance

The second source of systematic uncertainty is the event number. In different rigidity ranges, the antiproton signal number is determined with diverse backgrounds and different template fit methods. Therefore, it has to be calculated individually in different rigidity ranges.

In the low rigidity range, the antiproton signal is derived from a 2D template fit in 1/TOF-Beta and TRDLikelihood. A variation of the template fit range is used to estimate the template fit result. As introduced in section 4.4, the official result is chosen from the template fit range in 90% signal efficiency. To estimate the systematic uncertainty, the template fit is performed 342 times with signal efficiency 40% to 95%. For the first five points, the signal efficiency range is from 65% due to the low statistics. Then the RMS of the result distribution is chosen as the systematic error in each rigidity bin.

In the intermediate rigidity range, the same logic to calculate systematic uncertainty is used, but the difference is the template fit in intermediate rigidity is 1D template fit in TRDLikelihood. So in this range, the template fit is performed from 60% to 100% signal efficiency range.

In figure 4.29, an example of template fit results from different signal efficiency is shown. The rigidity bin is 2.15 to 2.4 GV, and the RMS of the results is used as the systematic error in this bin.

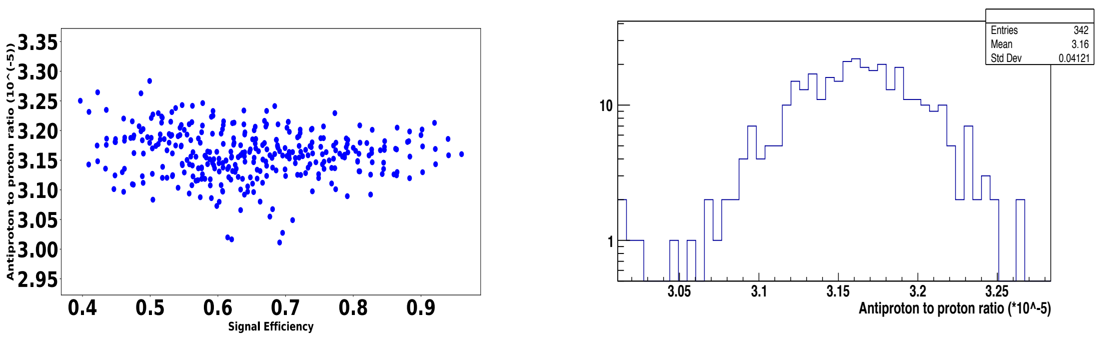

(a) (b)

Figure 4.29: The template fit result in 2.15 to 2.4 GV with signal efficiency from 40%. a). The template fit result distribution as a function of signal efficiency. b). The template fit result histogram. The RMS of the histogram is used as the systematic error.

In figure 4.30, the systematic uncertainty from the template fit range is shown. The absolute error is relatively stable at around 10^{-6}.

In the high rigidity range, the charge confused proton background rises dramatically with rigidity going up. The template of charge confused proton, which is taken from proton MC, becomes the primary source of systematic error, replacing the template fit range.

To estimate the charge confusion systematic error, the charge confusion level (CC Level) between MC and ISS data is used. The CC Level is defined as the charge confused proton number over the sum of charge confused proton number and charge correct proton number. In figure 4.31, the MC/data CC Level ratio is shown. The uncertainty band is derived with 68% C.L. and used as the variation of the CC Level, which transfers to charge confused proton number. Then the template fit in the high rigidity range is redone with a fixed charge confused proton number with the variation. This leads to antiproton numbers uncertainty

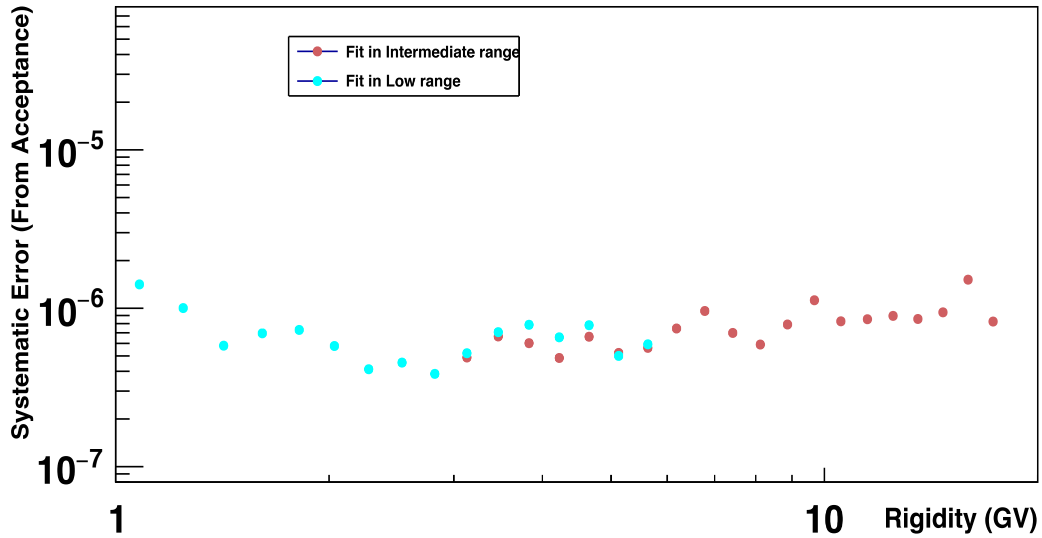

Figure 4.30: The systematic error from template fit range

due to charge confusion.

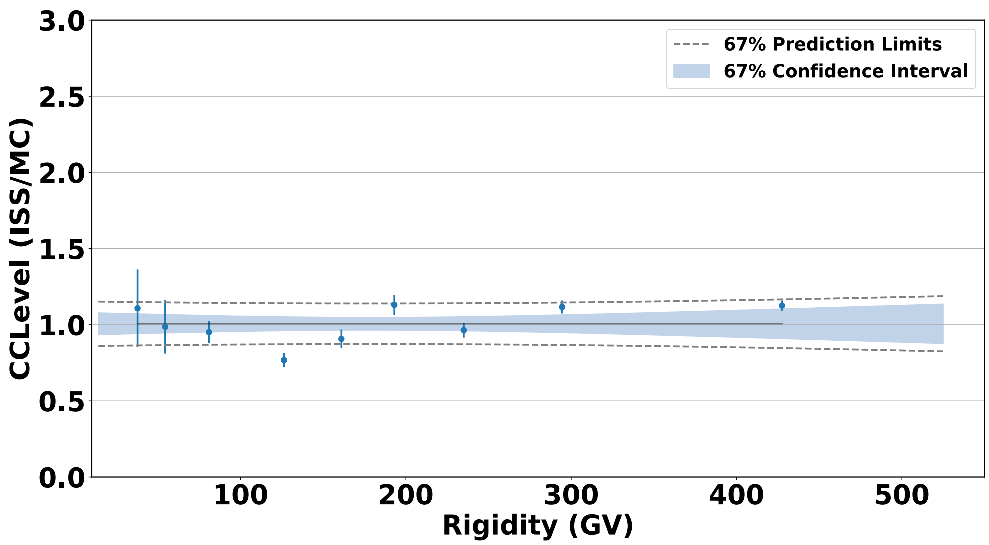

Figure 4.31: Data/MC charge confusion level ratio.

In figure 4.32 the systematic error due to charge confusion is shown.

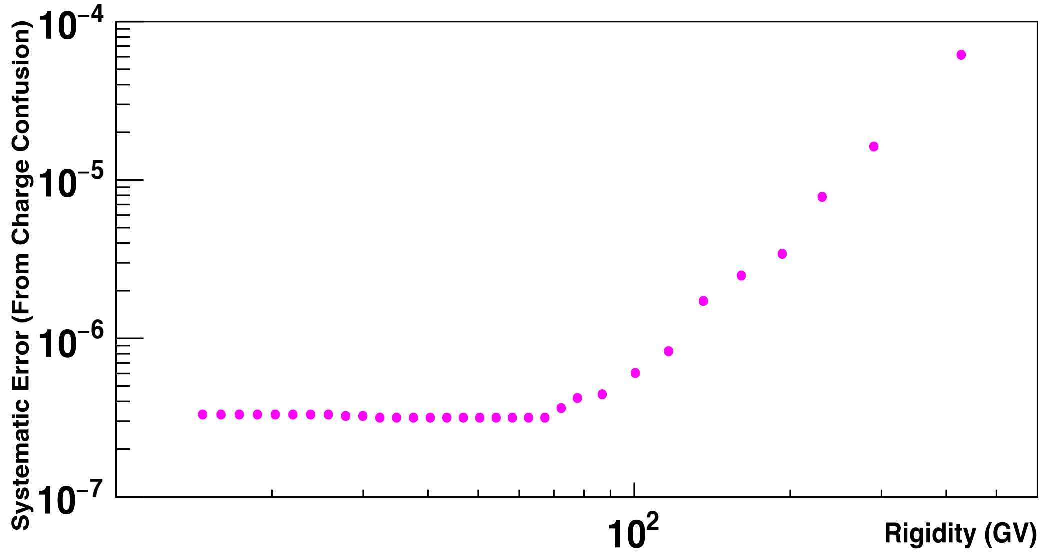

Figure 4.32: The systematic error from charge confusion

The different systematic errors are added quadratically to arrive at the total systematic error. In figure 4.33, the total systematic error is presented.

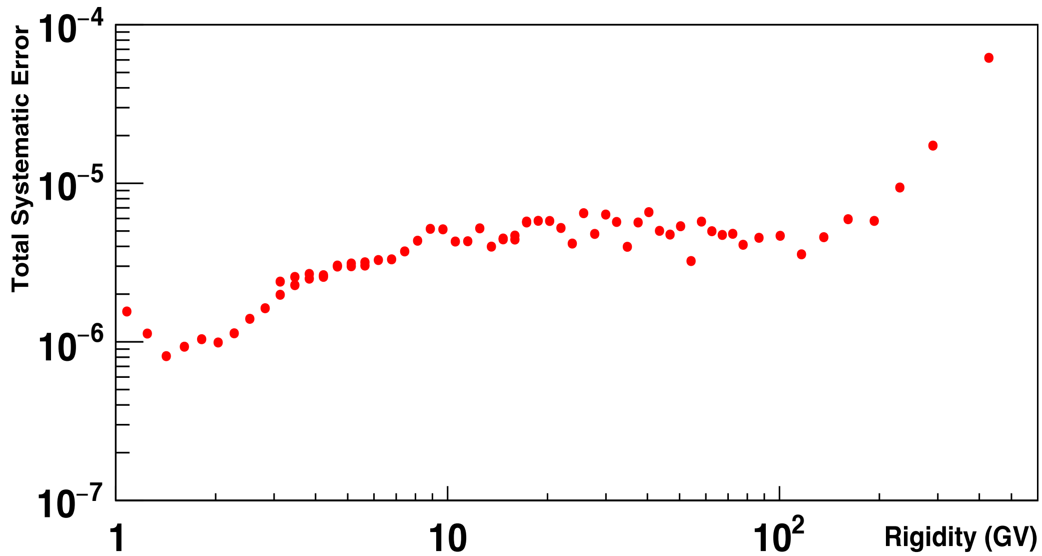

Figure 4.33: The total systematic error

The statistical error is directly taken from template fit in different rigidity ranges. The total error of the result is calculated by the square root of the sum of squares of statistical error and systematic error.

For the time dependent analysis, the same calculation way is used. Since the time dependent analysis is only performed below 20 GV. Therefore, only the result in the low and intermediate range is considered.

In figure 4.34, the systematic error in 1.92 to 2.4 GV in six Bartels Rotation time bin is shown as an example.

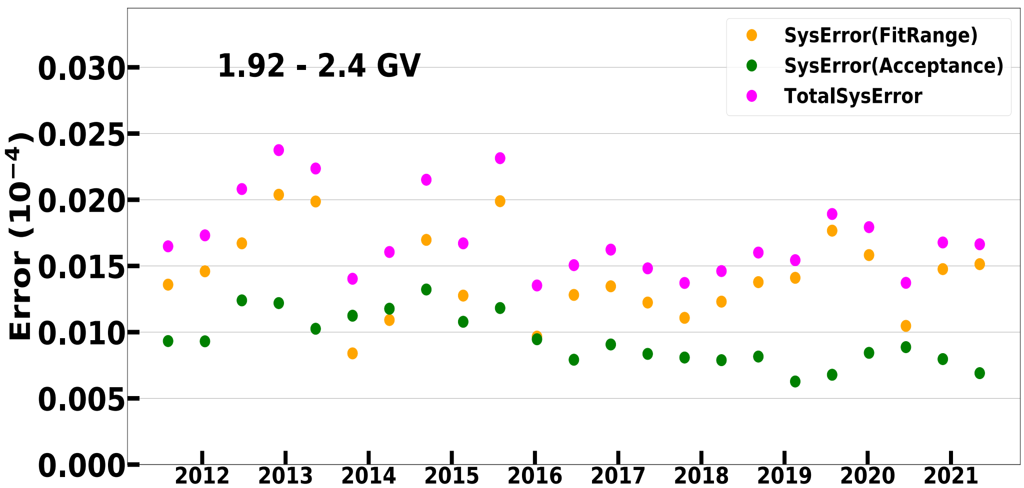

Figure 4.34: Systematic error of the antiproton to proton flux ratio in 1.92 to 2.4 GV in six Bartels Rotation time bin

BIBLIOGRAPHY

[1] NobelPrize.org (Nobel Media AB). Victor F. Hess - Facts, 2022. URL: https://www.nobelprize.org/prizes/physics/1936/hess/facts.

[2] NobelPrize.org (Nobel Media AB). Carl D. Anderson - Facts, 2022. URL: https://www.nobelprize.org/prizes/physics/1936/anderson/facts.

[3] NobelPrize.org (Nobel Media AB). The Nobel Prize in Physics 1959, 2022. URL: https://www.nobelprize.org/prizes/physics/1959/summary.

[4] O. Adriani et al. Measurement of the flux of primary cosmic ray antiprotons with energies of 60-MeV to 350-GeV in the PAMELA experiment. *Pisma Zh. Eksp. Teor. Fiz.*, 96:693–699, 2012. DOI: 10.1134/S002136401222002X.

[5] Kenneth Greisen. End to the Cosmic-Ray Spectrum? *Phys. Rev. Lett.*, 16:748–750, Apr 1966. DOI: 10.1103/PhysRevLett.16.748.

[6] G T Zatsepin and V A Kuz'min. Upper Limit of the Spectrum of Cosmic Rays. *Soviet Journal of Experimental and Theoretical Physics Letters*, 4:78, Aug 1966. URL: https://www.osti.gov/biblio/4515382.

[7] Dinu Al. Detection of a Cosmic Ray with Measured Energy Well beyond the Expected Spectral Cutoff due to Cosmic Microwave Radiation. *Astrophysical Journal*, 441:144, Mar 1995. DOI: 10.1086/175344.

[8] R. Abbasi et al. Indications of Intermediate-Scale Anisotropy of Cosmic Rays with Energy Greater than 57 EeV In the Northern sky measured with the surface detector of the telescope array experiment. *The Astrophysical Journal*, 790(2):L21, Jul 2014. DOI: 10.1088/2041-8205/790/2/l21.

[9] Alicia Lopez Oramas. Multi-year Campaign of the Gamma-Ray Binary LS I $+61^{\circ}$ 303 and Search for VHE Emission from Gamma-Ray Binary Candidates with the MAGIC Telescopes. PhD thesis, Universitat Autonoma de Barcelona, Apr 2015. DOI: 10.13140/RG.2.1.4140.4969.

[10] R. L. Workman and Others (Particle Data Group). Review of Particle Physics. *PTEP*, 2022:p.083C01, 2022. DOI: 10.1093/ptep/ptac097.

[11] Alessandra Pacini. Cosmic rays: Bringing messages from the sky to the Earth's surface. *Revista Brasileira de Ensino de Fisica*, 39, Jan 2017. DOI: 10.1590/1806-9126-RBEF-2016-0168.

[12] W. Baade and F. Zwicky. Cosmic Rays from Super-novae. *Proceedings of the National Academy of Sciences of the United States of America*, 20(5):259–263, 1934. URL:

http://www.jstor.org/stable/86841.

[13] Massimo Turatto. *Classification of* Supernovae, pages 21–36. Springer Berlin Heidelberg, Berlin, Heidelberg, 2003. DOI: 10.1007/3-540-45863-8_3.

[14] Stephen P. Reynolds. Supernova Remnants at High Energy. *Annual Review of Astronomy and Astrophysics*, 46(1):89–126, 2008. DOI: 10.1146/annurev.astro.46.060407.145237.

[15] Malcolm S. Longair. High Energy Astrophysics. UK: Cambridge University Press, 2011. URL: https://ui.adsabs.harvard.edu/abs/2011hea..book.....L.

[16] ENRICO Fermi. On the Origin of the Cosmic Radiation. *Phys. Rev.*, 75:1169–1174, Apr 1949. DOI: 10.1103/PhysRev.75.1169.

[17] T. Gold, F. G. Smith, and A. W. Wolfendale. Pulsars and the Origin of Cosmic Rays and Discussion. *Philosophical Transactions of the Royal Society of London. Series A, Mathematical and Physical Sciences*, 277(1270):453–461, 1975. URL: http://www.jstor.org/stable/74493.

[18] Bednarek, W. and Bartosik, M. Cosmic rays from Galactic pulsars. *Astronomy & Astrophysics*, 423(2):405–413, 2004. DOI: 10.1051/0004-6361:20047005.

[19] J Arons. Pulsar wind nebulae as cosmic pevatrons: A current sheet's tale. *Space Sci Rev*, 173:341–367, 2012. DOI: 10.1007/s11214-012-9885-1.

[20] A. R. Bell. Cosmic ray acceleration in pulsar-driven supernova remnants. *Monthly Notices of the Royal Astronomical Society*, 257(3):493–500, Aug 1992. DOI: 10.1093/mnras/257.3.493.

[21] Dan Hooper, Pasquale Blasi, and Pasquale Dario Serpico. Pulsars as the sources of high energy cosmic ray positrons. *Journal of Cosmology and Astroparticle Physics*, 2009(01):025, Jan 2009. DOI: 10.1088/1475-7516/2009/01/025.

[22] R. Cowsik. Positrons and Antiprotons in Galactic Cosmic Rays. *Annual Review of Nuclear and Particle Science*, 66(1):297–319, 2016. DOI: 10.1146/annurev-nucl-102115-044851.

[23] Jan Heisig. Cosmic-ray antiprotons in the ams-02 era: A sensitive probe of dark matter. *Modern Physics Letters A*, 36(05):2130003, 2021. DOI: 10.1142/S0217732321300032.

[24] Martin Wolfgang Winkler. Cosmic ray antiprotons at high energies. *Journal of Cosmology and Astroparticle Physics*, 2017(02):048–048, Feb 2017. DOI: 10.1088/1475-7516/2017/02/048.

[25] Rolf Kappl and Martin Wolfgang Winkler. The cosmic ray antiproton background for AMS-02. *Journal of Cosmology and Astroparticle Physics*, 2014(09):051–051, Sep 2014. DOI: 10.1088/1475-7516/2014/09/051.

[26] Andrew W. Strong, Igor V. Moskalenko, and Vladimir S. Ptuskin. Cosmic-Ray Propagation and Interactions in the Galaxy. *Annual Review of Nuclear and Particle Science*, 57(1):285–327, 2007. DOI: 10.1146/annurev.nucl.57.090506.123011.

[27] Igor V. Moskalenko. Galprop: modeling cosmic ray propagation and associated interstellar emissions, 2011. DOI: 10.48550/ARXIV.1105.4921.

[28] David Maurin. usine: Semi-analytical models for Galactic cosmic-ray propagation. *Computer Physics Communications*, 247:106942, 2020. DOI: 10.1016/j.cpc.2019.106942.

[29] Carmelo Evoli, Daniele Gaggero, Andrea Vittino, Giuseppe Di Bernardo, Mattia Di Mauro, Arianna Ligorini, Piero Ullio, and Dario Grasso. Cosmic-ray propagation with DRAGON2: I. numerical solver and astrophysical ingredients. *Journal of Cosmology and Astroparticle Physics*, 2017(02):015–015, Feb 2017. DOI: 10.1088/1475-7516/2017/02/015.

[30] V. S. Ptuskin, O. N. Strelnikova, and L. G. Sveshnikova. On leaky-box approximation to GALPROP. *Astropart. Phys.*, 31:284–289, 2009. DOI: 10.1016/j.astropartphys.2009.02.004.

[31] E. N. Parker. Dynamics of the Interplanetary Gas and Magnetic Fields. *Astrophysical Journal*, 128:664, Nov 1958. DOI: 10.1086/146579.

[32] Christopher T. Russell. The Solar Wind and Magnetospheric Dynamics. In *Correlated Interplanetary and Magnetospheric Observations*, pages 3–47, Dordrecht, 1974. Springer Netherlands. DOI: 10.1007/978-94-010-2172-2_1.

[33] M.J. Owens and R.J. Forsyth. The Heliospheric Magnetic Field. *Living Rev. Sol. Phys.*, 10, Nov 2013. DOI: 10.12942/lrsp-2013-5.

[34] A. J. Dessler. Solar wind and interplanetary magnetic field. *Reviews of Geophysics*, 5(1):1–41, 1967. DOI: 10.1029/RG005i001p00001.

[35] R Cowen. Voyager 1 has reached interstellar space. *Nature*, 2013. DOI: 10.1038/nature.2013.13735.

[36] NASA. Solar wind at voyager 1, 2012. Retrieved 16:20, July 20, 2022 from: https://commons.wikimedia.org/wiki/File:Solar_wind_at_Voyager_1.png.

[37] David H. Hathaway. The Solar Cycle. *Living Reviews in Solar Physics*, 7(1):1, Dec

2010. DOI: 10.12942/lrsp-2010-1.

[38] Carsten Jorgensen, Christoffer Karoff, Senthamizh Pavai Valliappan, and Rainer Arlt. Christian Horrebow's Sunspot Observations – I. Life and Published Writings. *Solar Physics*, Jun 2019. DOI: 10.1007/s11207-019-1465-z.

[39] Christoffer Karoff, Carsten Jorgensen, Senthamizh Pavai Valliappan, and Rainer Arlt. Christian Horrebow's Sunspot Observations – II. Construction of a Record of Sunspot Positions. *Solar Physics*, 294, Jun 2019. DOI: 10.1007/s11207-019-1466-y.

[40] Eddie Ross and William J. Chaplin. The behaviour of galactic cosmic ray intensity during solar activity cycle 24. *Solar Physics*, 294(1):8, Jan 2019. DOI: 10.1007/s11207-019-1397-7.

[41] EA Bogomolov, ND Lubyanaya, VA Romanov, SV Stepanov, and MS Shulakova. A stratospheric magnetic spectrometer investigation of the singly charged component spectra and composition of the primary and secondary cosmic radiation. In *International Cosmic Ray Conference*, volume 1, page 330, 1979.

[42] R. L. Golden, S. Horan, B. G. Mauger, G. D. Badhwar, J. L. Lacy, S. A. Stephens, R. R. Daniel, and J. E. Zipse. Evidence for the existence of cosmic-ray antiprotons. *Phys. Rev. Lett.*, 43:1196–1199, Oct 1979. DOI: 10.1103/PhysRevLett.43.1196.

[43] M. Nozaki. BESS-Polar. *Nuclear Instruments and Methods in Physics Research Section B: Beam Interactions with Materials and Atoms*, 214:110–115, 2004. DOI: 10.1016/j.nimb.2003.08.005.

[44] T. Yoshida, A. Yamamoto, and J. et al. Mitchell. Bess-polar experiment. *Life sciences and space research*, 33(10):1755–1762, 2004. DOI: 10.1016/j.asr.2003.05.017.

[45] K. Abe et al. Measurement of the cosmic-ray low-energy antiproton spectrum with the first BESS-Polar Antarctic flight. *Physics Letters B*, 670(2):103–108, 2008. DOI: 10.1016/j.physletb.2008.10.053.

[46] K. Abe et al. Measurement of the Cosmic-Ray Antiproton Spectrum at Solar Minimum with a Long-Duration Balloon Flight over Antarctica. *Phys. Rev. Lett.*, 108:051102, Jan 2012. DOI: 10.1103/PhysRevLett.108.051102.

[47] A M Galper et al. The PAMELA experiment: a decade of Cosmic Ray Physics in space. *Journal of Physics: Conference Series*, 798:012033, Jan 2017. DOI: 10.1088/1742-6596/798/1/012033.

[48] O. Adriani et al. (PAMELA Collaboration). New Measurement of the Antiproton-to-Proton Flux Ratio up to 100 GeV in the Cosmic Radiation. *Phys. Rev. Lett.*, 102:051101, Feb 2009. DOI: 10.1103/PhysRevLett.102.051101.

[49] O. Adriani et al. (PAMELA Collaboration). PAMELA Results on the Cosmic-Ray Antiproton Flux from 60 MeV to 180 GeV in Kinetic Energy. *Phys. Rev. Lett.*, 105:121101, Sep 2010. DOI: 10.1103/PhysRevLett.105.121101.

[50] M. Aguilar et al. (AMS Collaboration). Antiproton Flux, Antiproton-to-Proton Flux Ratio, and Properties of Elementary Particle Fluxes in Primary Cosmic Rays Measured with the Alpha Magnetic Spectrometer on the International Space Station. *Phys. Rev. Lett.*, 117:091103, Aug 2016. DOI: 10.1103/PhysRevLett.117.091103.

[51] S. et al. Ahlen. An antimatter spectrometer in space. *Nuclear Instruments and Methods in Physics Research Section A: Accelerators, Spectrometers, Detectors and Associated Equipment*, 350(1):351–367, 1994. DOI: 10.1016/0168-9002(94)91184-3.

[52] Roberto Battiston. The antimatter spectrometer (AMS-02): A particle physics detector in space. *Nuclear Instruments and Methods in Physics Research Section A: Accelerators, Spectrometers, Detectors and Associated Equipment*, 588(1):227–234, 2008. DOI: 10.1016/j.nima.2008.01.044.

[53] M Aguilar et al. The Alpha Magnetic Spectrometer (AMS) on the International Space Station: Part I - results from the test flight on the space shuttle. *Physics Reports*, 366(6):331–405, 2002. DOI: 10.1016/S0370-1573(02)00013-3.

[54] Roskosmos. STS-91 PLB, 1998. Retrieved 16:20, July 20, 2022 from: https://commons.wikimedia.org/wiki/File:STS-91_PLB.jpg.

[55] NASA/Crew-2. View of the ISS taken during crew-2 flyaround (iss066-e-081311), 2021. Retrieved 16:20, July 20, 2022 from: https://commons.wikimedia.org/wiki/File:View_of_the_ISS_taken_during_Crew-2_flyaround_(ISS066-E-081311).jpg.

[56] Zoe Budrikis. A decade of AMS-02. *Nature Reviews Physics*, 3(5):308–308, Jan 2021. DOI: 10.1038/s42254-021-00320-7.

[57] Fabian Machate. *Study for large acceptance electron analysis with the Alpha Magnetic Spectrometer on the International Space Station*. Dissertation, RWTH Aachen University, Aachen, 2021. DOI: 10.18154/RWTH-2021-09976.

[58] AMS Collaboration. The Alpha Magnetic Spectrometer on the International Space Station, 2022. URL: https://ams02.space.

[59] V. L. Ginzburg and I. M. Frank. Radiation of a uniformly moving electron due to its transition from one medium into another. *J. Phys. (USSR)*, 9:353–362, 1945.

[60] M. Heil et al. Operations and Alignment of the AMS-02 Transition Radiation Detector. In *33rd International Cosmic Ray Conference*, page 1232, 2013. URL:

https://galprop.stanford.edu/elibrary/icrc/2013/papers/icrc2013-1232.pdf.

[61] T. Siedenburg. The AMS TRD. A gasdetector designed for operation in space. *Nuclear Physics B - Proceedings Supplements*, 150:30–33, 2006. DOI: 10.1016/j.nuclphysbps.2004.06.001.

[62] Thomas Kirn. The AMS-02 TRD on the international space station. *Nuclear Instruments and Methods in Physics Research Section A: Accelerators, Spectrometers, Detectors and Associated Equipment*, 706:43–47, 2013. DOI: 10.1016/j.nima.2012.05.010.

[63] Jerzy Neyman, Egon Sharpe Pearson, and Karl Pearson. Ix. On the problem of the most efficient tests of statistical hypotheses. *Philosophical Transactions of the Royal Society of London. Series A, Containing Papers of a Mathematical or Physical Character*, 231(694-706):289–337, 1933. DOI: 10.1098/rsta.1933.0009.

[64] B. Blau, S.M. Harrison, H. Hofer, S.R. Milward, J.S.H. Ross, S.C.C. Ting, J. Ulbricht, and G. Viertel. The superconducting magnet of ams-02. *Nuclear Physics B - Proceedings Supplements*, 113(1):125–132, 2002. DOI: 10.1016/S0920-5632(02)01831-5.

[65] K. Lubelsmeyer et al. Upgrade of the Alpha Magnetic Spectrometer (AMS-02) for long term operation on the International Space Station (ISS). *Nuclear Instruments and Methods in Physics Research Section A: Accelerators, Spectrometers, Detectors and Associated Equipment*, 654(1):639–648, 2011. DOI: 10.1016/j.nima.2011.06.051.

[66] Pierre Erwan Saouter. Operation and Performance of AMS-02 Silicon Tracker. *PoS*, Vertex2014:028, 2015. DOI: 10.22323/1.227.0028.

[67] Sadakazu Haino. Performance of the AMS-02 silicon tracker in the ISS mission. *Nucl. Instrum. Meth. A*, 699:221–224, 2013. DOI: 10.1016/j.nima.2012.05.060.

[68] G. Ambrosi et al. Alignment of the AMS-02 Silicon Tracker. In *33rd International Cosmic Ray Conference*, page 1260, 2013. URL: https://ui.adsabs.harvard.edu/abs/2013ICRC...33..570A.

[69] B. Alpat et al. The internal alignment and position resolution of the ams-02 silicon tracker determined with cosmic-ray muons. *Nuclear Instruments and Methods in Physics Research Section A: Accelerators, Spectrometers, Detectors and Associated Equipment*, 613(2):207–217, 2010. DOI: 10.1016/j.nima.2009.11.065.

[70] V. Bindi et al. Calibration and performance of the AMS-02 time of flight detector in space. *Nucl. Instrum. Meth. A*, 743:22–29, 2014. DOI: 10.1016/j.nima.2014.01.002.

[71] V. Bindi, A. Contin, N. Masi, A. Oliva, F. Palmonari, L. Quadrani, and A. Tiseni. The time of flight detector of the AMS-02 experiment on the international space station. *Nucl. Instrum. Meth. A*, 718:478–480, 2013. DOI: 10.1016/j.nima.2012.11.061.

[72] V. Bindi, E. Choumilov, A. Contin, N. Masi, A. Oliva, F. Palmonari, L. Quadrani, and Q. Yan. The AMS-02 Time of Flight (TOF) System: Construction and Overall Performances in Space. In *International Cosmic Ray Conference*, volume 33 of *International Cosmic Ray Conference*, page 2298, Jan 2013. URL: https://ui.adsabs.harvard.edu/abs/2013ICRC...33.2298B.

[73] Hu Liu, J. Casaus, F. Giovacchini, A. Oliva, and X. Xia. The RICH detector of AMS-02: 5 years of operation in space. *Nucl. Instrum. Meth. A*, 876:5–8, 2017. DOI: 10.1016/j.nima.2016.12.011.

[74] R. Pereira. The AMS-02 RICH detector: Performance during ground-based data taking at CERN. *Nucl. Instrum. Meth. A*, 639:37–41, 2011. DOI: 10.1016/j.nima.2010.09.036.

[75] F. Giovacchini, J. Casaus, and A. Oliva. The AMS-02 RICH detector: Status and physics results. *Nuclear Instruments and Methods in Physics Research Section A: Accelerators, Spectrometers, Detectors and Associated Equipment*, 952:161797, 2020. DOI: 10.1016/j.nima.2019.01.024.

[76] F. Giovacchini. Performance in space of the AMS-02 RICH detector. *Nuclear Instruments and Methods in Physics Research Section A: Accelerators, Spectrometers, Detectors and Associated Equipment*, 766:57–60, 2014. DOI: 10.1016/j.nima.2014.04.036.

[77] Sylvie Rosier-Lees. Performance of the AMS02 electromagnetic calorimeter in space. *J. Phys. Conf. Ser.*, 404:012034, 2012. DOI: 10.1088/1742-6596/404/1/012034.

[78] M. Vecchi et al. The electromagnetic calorimeter of the AMS-02 experiment. In *Semaine de l'Astrophysique Francaise (SF2A 2012)*, Nice, France, Jun 2012. URL: http://hal.in2p3.fr/in2p3-00745677.

[79] C. Adloff et al. The AMS-02 lead-scintillating fibres Electromagnetic Calorimeter. *Nucl. Instrum. Meth. A*, 714:147–154, 2013. DOI: 10.1016/j.nima.2013.02.020.

[80] Marco Incagli. Performance of the AMS-02 Electromagnetic Calorimeter in Space. *PoS*, TIPP2014:025, 2014. DOI: 10.22323/1.213.0025.

[81] Manuela Vecchi, Kaiyuan Wu, and Yuan-Hann Chang. A 3-dimensional electromagnetic shower characterization and its application to AMS-02 pointing capability. In *33rd International Cosmic Ray Conference*, page 0653, 2013.

[82] Stefano Di Falco. Results of 2007 test beam of AMS-02 Electromagnetic Calorimeter. *Adv. Space Res.*, 45:112–122, 2010. DOI: 10.1016/j.asr.2009.08.005.

[83] G Gallucci and (for the AMS-02 ECAL group). Performance of the AMS-02 Electromagnetic Calorimeter in Space. *Journal of Physics: Conference Series*, 587:012028,

Feb 2015. DOI: 10.1088/1742-6596/587/1/012028.

[84] Ph. von Doetinchem, W. Karpinski, Th. Kirn, K. Luebelsmeyer, St. Schael, and M. Wlochal. The AMS-02 Anticoincidence Counter. *Nucl. Phys. B Proc. Suppl.*, 197:15–18, 2009. DOI: 10.1016/j.nuclphysbps.2009.10.025.

[85] T. Bruch and W. Wallraff. The Anti-Coincidence Counter shield of the AMS tracker. *Nucl. Instrum. Meth. A*, 572:505–507, 2007. DOI: 10.1016/j.nima.2006.10.376.

[86] A. Basili, V. Bindi, D. Casadei, G. Castellini, A. Contin, A. Kounine, M. Lolli, F. Palmonari, and L. Quadrani. The TOF-ACC flight electronics for the fast trigger and time of flight of the AMS-02 cosmic ray spectrometer. *Nucl. Instrum. Meth. A*, 707:99–113, 2013. DOI: 10.1016/j.nima.2012.12.089.

[87] Ph. von Doetinchem, Th. Kirn, K. Luebelsmeyer, and St. Schael. The Anticoincidence Counter System of AMS-02, 2009. DOI: 10.48550/ARXIV.0906.1068.

[88] Rene Brun and Fons Rademakers. Root - An object oriented data analysis framework. *Nuclear Instruments and Methods in Physics Research Section A: Accelerators, Spectrometers, Detectors and Associated Equipment*, 389(1):81–86, 1997. DOI: 10.1016/S0168-9002(97)00048-X.

[89] Bastian Beischer. *Measurement of high energy gamma rays from 200 MeV to 1 TeV with the Alpha Magnetic Spectrometer on the International Space Station*. Dissertation, RWTH Aachen University, Aachen, 2020. DOI: 10.18154/RWTH-2020-06535.

[90] M. Aguilar et al. (AMS Collaboration). Precision Measurement of the Proton Flux in Primary Cosmic Rays from Rigidity 1 GV to 1.8 TV with the Alpha Magnetic Spectrometer on the International Space Station. *Phys. Rev. Lett.*, 114:171103, Apr 2015. DOI: 10.1103/PhysRevLett.114.171103.

[91] J. Bartels. Twenty-seven day recurrences in terrestrial-magnetic and solar activity, 1923-1933. *Terrestrial Magnetism and Atmospheric Electricity*, 39(3):201–202a, 1934. DOI: 10.1029/TE039i003p00201.

[92] S. Agostinelli et al. GEANT4–a simulation toolkit. *Nucl. Instrum. Meth. A*, 506:250–303, 2003. DOI: 10.1016/S0168-9002(03)01368-8.

[93] J. Allison et al. Recent developments in Geant4. *Nucl. Instrum. Meth. A*, 835:186–225, 2016. DOI: 10.1016/j.nima.2016.06.125.

[94] Paolo Zuccon. AMS-02 Track reconstruction and rigidity measurement. In *33rd International Cosmic Ray Conference*, page 1064, 2013. URL: https://s3.cern.ch/inspire-prod-files-7/71c48c76263c1f7bee2621c779ba3320.

[95] Helge Voss, Andreas Hocker, Jorg Stelzer, and Fredrik Tegenfeldt. TMVA, the toolkit for multivariate data analysis with ROOT. In XI International Workshop on Advanced Computing and Analysis Techniques in Physics Research, volume 50, page 040. SISSA Medialab, 2009. DOI: 10.22323/1.050.0040.

[96] J.D. Sullivan. Geometric factor and directional response of single and multi-element particle telescopes. *Nuclear Instruments and Methods*, 95(1):5–11, 1971. DOI: 10.1016/0029-554X(71)90033-4.

[97] Nikolas Zimmermann. *Precision measurement of the cosmic-ray electron and positron fluxes as a function of time and energy with the Alpha Magnetic Spectrometer on the International Space Station*. Dissertatison, RWTH Aachen University, Aachen, 2020. DOI: 10.18154/RWTH-2020-02650.

[98] Carl Stormer. The polar aurora. *Quarterly Journal of the Royal Meteorological Society*, 82(351):115–115, 1956. DOI: 10.1002/qj.49708235123.

[99] G. D'Agostini. A multidimensional unfolding method based on Bayes' theorem. *Nuclear Instruments and Methods in Physics Research Section A: Accelerators, Spectrometers, Detectors and Associated Equipment*, 362(2):487–498, 1995. DOI: 10.1016/0168-9002(95)00274-X.

[100] Tim Adye. Unfolding algorithms and tests using RooUnfold. In *PHYSTAT 2011*, pages 313–318, Geneva, 2011. CERN. DOI: 10.5170/CERN-2011-006.313.

[101] AMS Collaboration. The Alpha Magnetic Spectrometer (AMS) on the international space station: Part II – Results from the first seven years. *Physics Reports*, 894:1–116, 2021. DOI: 10.1016/j.physrep.2020.09.003.